Applicability of the $\mathbf{k}\cdot\mathbf{p}$ method to the electronic structure of quantum dots

Huaxiang Fu, Lin-Wang Wang, and Alex Zunger
National Renewable Energy Laboratory, Golden, Colorado 80401
(Received 18 September 1997)

The $\mathbf{k}\cdot\mathbf{p}$ method has become the ''standard model'' for describing the electronic structure of nanometer-size quantum dots. In this paper we perform parallel $\mathbf{k}\cdot\mathbf{p}$ (6×6 and 8×8) and direct-diagonalization pseudopotential studies on spherical quantum dots of an ionic material—CdSe, and a covalent material—InP. By using an equivalent input in both approaches, i.e., starting from a given atomic pseudopotential and deriving from it the Luttinger parameters in $\mathbf{k}\cdot\mathbf{p}$ calculation, we investigate the effect of the different underlying wavefunction representations used in $\mathbf{k}\cdot\mathbf{p}$ and in the more exact pseudopotential direct diagonalization. We find that (i) the 6×6 $\mathbf{k}\cdot\mathbf{p}$ envelope function has a distinct (odd or even) parity, while atomistic wave function is parity-mixed. The 6×6 $\mathbf{k}\cdot\mathbf{p}$ approach produces an incorrect order of the highest valence states for both InP and CdSe dots: the p-like level is above the s-like level. (ii) It fails to reveal that the second conduction state in small InP dots is folded from the L point in the Brillouin zone. Instead, all states in $\mathbf{k}\cdot\mathbf{p}$ are described as Γ-like. (iii) The $\mathbf{k}\cdot\mathbf{p}$ overestimates the confinement energies of both valence states and conduction states. A wavefunction projection analysis shows that the principal reasons for these $\mathbf{k}\cdot\mathbf{p}$ errors in dots are (a) use of restricted basis set, and (b) incorrect *bulk* dispersion relation. Error (a) can be reduced only by increasing the number of basis functions. Error (b) can be reduced by altering the $\mathbf{k}\cdot\mathbf{p}$ implementation so as to bend upwards the second lowest bulk band, and to couple the conduction band into the s-like dot valence state. Our direct diagonalization approach provides an accurate and practical replacement to the standard model in that it is rather general, and can be performed simply on a standard workstation. [S0163-1829(98)03112-9]

I. INTRODUCTION

Nanometer-size semiconductor quantum dots can now be made either by colloidal techniques[1–8] or by controlled coarsening of thin films grown via the Stranski-Krastanov mode.[9–12] Colloidally-grown dots of CdSe,[1–4] InP,[5–7] or InAs (Ref. 8) are nearly spherical, unstrained objects with diameters ranging from 20 to 70 Å, whose surfaces are passivated by organic ligands. The size distribution is so uniform that up to 10 excited electron-hole states can be observed in photoluminescence excitation spectroscopy.[2,8] Quantum dots fabricated by controlled coarsening (''self-assembled''), on the other hand, appear in flattened pyramidal (or sometimes pancake) shapes with confining dimensions (height) of 50–150 Å. These are strained objects passivated by a (lattice-mismatched) semiconductor barrier (e.g., InAs/GaAs). Typically, 1–3 excited electron-hole states have been observed.[11]

The emergence of rich spectroscopic signatures in both classes of semiconductor quantum dots has prompted a number of recent attempts at interpreting their electronic structure.[1–4,7–10,12–16] The ''standard model'' used almost universally to this end is the $\mathbf{k}\cdot\mathbf{p}$ effective-mass approach.[17–19] In this method, a number (N_b) of bulk Bloch bands at the Brillouin-zone center (Γ states) are used to expand the wave functions of the dot, and matrix elements are determined empirically via fitting the observed bulk dispersion curves. The electronic structure of the unstrained, spherical colloidal dots has been successfully interpreted via the $N_b=6$ bands $\mathbf{k}\cdot\mathbf{p}$ approach whose free parameters are fitted to the measured spectrum of the quantum *dots* itself.[2,4] The electronic structure of the strained pyramidal dots has been interpreted via a single band effective-mass model,[12] a single heavy-hole model,[10] a 4-band $\mathbf{k}\cdot\mathbf{p}$ model,[13] and an 8-band $\mathbf{k}\cdot\mathbf{p}$ model,[14] with parameters fitted to the measured *bulk* properties.

The absence of translational periodicity in all three dimensions, the existence of carrier quantum confinement in small volumes, and the appearance of inhomogeneous interfacial strain[20] and surface states,[21] all contribute to create extensive coupling between bulk Bloch states in forming the wave functions of quantum dots. Current $\mathbf{k}\cdot\mathbf{p}$ methods[2,7,10,12–16] approximate this massive coupling via a restricted basis set of just a few (2–8), Γ-like bulk Bloch bands. Since the excitation energies are sometimes fitted directly to experiment on quantum dots,[2,4] agreement with experiment, by itself, does not always provide a test to the adequacy of the representation. Thus, independent tests, free from fitting the target results, are needed in order to understand the spectroscopy of nanostructures.

In the cases of (i) three-dimensional (3D)-periodic bulk solids,[22–24] and (ii) 2D-periodic quantum wells[23,25,26] or superlattices, such direct tests of the $\mathbf{k}\cdot\mathbf{p}$ method do exist. In these cases, the energy bands obtained via a direct diagonalization (i.e., converged N_b) of the electronic Hamiltonian (e.g., pseudopotential[23,24] or tight-binding[25,26]) are contrasted with standard $\mathbf{k}\cdot\mathbf{p}$ predictions whose input (''Luttinger'') parameters are derived, for consistency, from the same underlying Hamiltonian. Such tests have shown how well the $\mathbf{k}\cdot\mathbf{p}$ method works near the Γ-point (from which its parameters are drawn), and how its performance deteriorates when called upon to describe states whose wave functions have significant off-Γ components. The ability of a set of N_b Bloch functions at Γ-point $\{u_{m,\Gamma}(\mathbf{r})\}$ to represent a single Bloch orbital $u_{n,\mathbf{k}\neq0}(\mathbf{r})$ away from Γ can be measured by

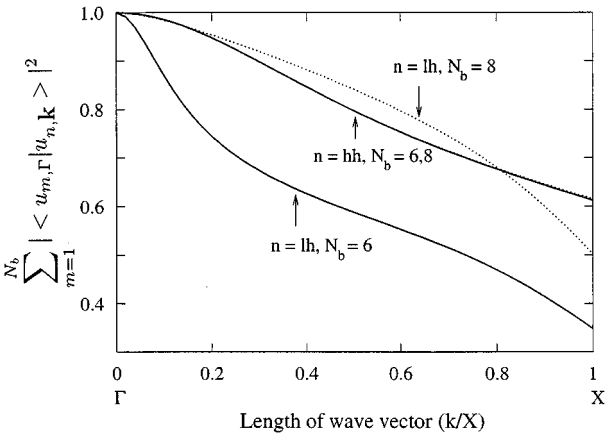

FIG. 1. The overlap $P_n^{(N_b)}(\mathbf{k})=\Sigma_{m=1}^{N_b}|\langle u_{m,\Gamma}|u_{n,\mathbf{k}}\rangle|^2$ between the $\mathbf{k}\neq 0$ Bloch function $u_{n,\mathbf{k}}(\mathbf{r})$ and the Γ-like states $\{u_{m,\Gamma}(\mathbf{r})\}$. The closer the overlap is to 1, the better the set of N_b Γ-like states can describe a $\mathbf{k}\neq 0$ state. All basis functions are calculated by pseudopotential direct diagonalization (solid lines: $N_b=6$; dotted lines: $N_b=8$).

$P_n^{(N_b)}(\mathbf{k})=\Sigma_{m=1}^{N_b}|\langle u_{m,\Gamma}|u_{n,\mathbf{k}}\rangle|^2$. The closer $P_n^{(N_b)}(\mathbf{k})$ is to 1, the more complete is the representation of $u_{n,\mathbf{k}\neq 0}(\mathbf{r})$ via the set $\{u_{m,\Gamma}(\mathbf{r})\}$. Figure 1 shows (neglecting spin-orbit coupling) for zincblende bulk InP how its light-hole (lh) and heavy-hole (hh) bands at $\mathbf{k}\neq 0$ along (100) direction can be expanded by $N_b=6$ or by $N_b=8$ Γ bands. We see that if $N_b=6$ Γ bands (two lh and four hh) are used, only 70% of the $\mathbf{k}=2\pi/a(0.2,0,0)$ lh character can be captured. The error increases rapidly as one moves further away from $\mathbf{k}=0$. For the hh state, $P_{hh}^{(N_b)}(\mathbf{k})$ is almost the same for $N_b=6$ and $N_b=8$ since the hh state does not couple with the conduction band. From Fig. 1, we see that even for the 3D bulk, the error $1-P_n^{(N_b)}(\mathbf{k})$ of representing the wave function away from Γ by a small number of Γ-like bulk bases grows rapidly as the wave vector $\mathbf{k}$ moves away from Brillouin-zone center. A recent study[27] has shown that, given that the parameters of the $\mathbf{k}\cdot\mathbf{p}$ method are usually fitted to the 3D-periodic bulk solid, its errors increase in the sequence of 3D bulk→2D wells→superlattices→1D quantum wires→0D quantum dots. However, only the first two of this sequence (3D and 2D) have been studied. The adequacy of the currently used $\mathbf{k}\cdot\mathbf{p}$ models to describe the spectroscopy of 0*D quantum dots* has thus far not been examined.

In spite of the expected breakdown of the small basis $\mathbf{k}\cdot\mathbf{p}$ method for small dot sizes, a large number of $\mathbf{k}\cdot\mathbf{p}$ calculations[1–4,7–10,12–16] exist on dots down to the size of 20 Å diameter. Sometimes such calculations offer a distinct physical explanation to some important experimental phenomena. For example, $\mathbf{k}\cdot\mathbf{p}$ theory[7,15] predicted that the top valence state of InP dots has *p*-envelope symmetry, and is thus dipole forbidden to the *s*-envelope lowest conduction state. This prediction has been used to explain the observed long radiative lifetime,[7] and is also appealing to explain the observed photoluminescence red shift.[6] However, a direct diagonalization calculation (see below) shows that the top valence state has *s*-symmetry, so a fundamentally different physical explanation has to be sought for the above experimental observations.[28]

In considering the adequacy of the $\mathbf{k}\cdot\mathbf{p}$ method, three issues will be studied: (i) What are the dependences of energy level spacing and wave functions of dots on quantum sizes? (ii) What are the order and symmetry of dot valence states? Does the top valence state have a *s*-like or *p*-like envelope symmetry? (iii) Why does the ''standard $\mathbf{k}\cdot\mathbf{p}$ model'' appear to work better for CdSe dots[2] than for InP (Ref. 7) and InAs?[8]

In this paper we perform parallel $\mathbf{k}\cdot\mathbf{p}$ and direct-diagonalization (pseudopotential) studies on spherical, unstrained quantum dots of an ionic material—CdSe, and a covalent material—InP. The inputs to both approaches are equivalent—we start from a given atomic pseudopotential and derive from it the Luttinger parameters needed as input to the $\mathbf{k}\cdot\mathbf{p}$ calculation on the electronic structure of dot. The comparison between the results thus reflects the different underlying wave function representations used by the $\mathbf{k}\cdot\mathbf{p}$ and the direct-diagonalization approach. We will see that the direct-diagonalization pseudopotential approach not only offers a way to analyze the $\mathbf{k}\cdot\mathbf{p}$, but is also a viable, more accurate, and flexible replacement to the $\mathbf{k}\cdot\mathbf{p}$ approach.

II. DIRECT-DIAGONALIZATION APPROACH TO BULK SOLIDS AND DOTS

The single-particle electronic structure of bulk-periodic solids or nanostructures is generally described by solving the Schrodinger equation:

$$\left[\frac{\mathbf{P}^2}{2m_0}+V(\mathbf{r})\right]\psi(\mathbf{r})=\epsilon\psi(\mathbf{r}). \tag{1}$$

The potential $V(\mathbf{r})$ could be computed self-consistently from the occupied states (e.g., the density-functional formalism[29]), or it could be approximated as a superposition of screened atomic potentials[30]

$$V(\mathbf{r})=\sum_{\alpha}\sum_{\mathbf{R}} v_{\alpha}(\mathbf{r}-\mathbf{R}-\mathbf{d}_{\alpha}) \tag{2}$$

for atom species α at basis site $\mathbf{d}_{\alpha}$ in cell $\mathbf{R}$. Equation (1) is usually solved by expanding $\psi(\mathbf{r})$ in some fixed basis set. For periodically repeated units, where $\psi(\mathbf{r})$ can be written in a Bloch form

$$\psi_{n\mathbf{k}}(\mathbf{r})=e^{i\mathbf{k}\cdot\mathbf{r}}u_{n\mathbf{k}}(\mathbf{r}), \tag{3}$$

a natural choice is to expand ψ in plane waves of reciprocal lattice vector $\mathbf{G}$:

$$\psi_{n\mathbf{k}}(\mathbf{r})=e^{i\mathbf{k}\cdot\mathbf{r}}\sum_{\mathbf{G}}^{\mathbf{G}_{\max}} C_{n\mathbf{k}}(\mathbf{G})e^{i\mathbf{G}\cdot\mathbf{r}}, \tag{4}$$

where $\mathbf{G}_{\max}$ is the cutoff of basis.

It is now straightforward to compute the screened pseudopotential $v_\alpha(\mathbf{r})$ from an atomistic mean-field electronic theory (e.g., density functional)[31,32] and to solve Eqs. (1) and (2) by a standard diagonalization method.[33] However, in this approach, the computational effort scales as the *cube* power of the number of atoms per unit cell (due to the need to orthogonalize each ψ_i to the lower states), so the method is limited to small systems containing <100 atoms per cell. Another approach is thus needed for quantum dots with $\sim 30-50$ Å diameter ($\approx 1000-5000$ atoms). We propose to build on the fact that in such nanostructures one is often interested only in the states near the valence-band maximum (VBM) and the conduction-band minimum (CBM). Hence, it makes no computational sense to have to orthogonalize these states to many lower-energy states that are physically uninteresting. It is more reasonable[34] to ''fold'' the spectrum of Eq. (1) around a reference energy $\epsilon_{\rm ref}$

$$\left[\frac{\mathbf{p}^2}{2m_0}+V(\mathbf{r})-\epsilon_{\rm ref}\right]^2\psi(\mathbf{r})=(\epsilon-\epsilon_{\rm ref})^2\psi(\mathbf{r}), \tag{5}$$

so that the lowest eigenvalue is now the one nearest to $\epsilon_{\rm ref}$. By placing $\epsilon_{\rm ref}$ in the region of physical interest (the band gap), one can thus find the highest occupied dot orbit (HODO) and the lowest unoccupied dot orbit (LUDO) without having to search and orthogonalize many lower eigenstates that are now shifted outside the ''window of interest.'' This linearly-scaling ''folded spectrum method'' has been applied[34–36] to 10^3-10^5 atom nanostructures using plane-wave bases [Eq. (4)] and screened pseudopotential [Eq. (2)]. We will refer to the approach of Eqs. (1)–(5) as ''direct diagonalization.''

A more conventional and more frequently used approach is the $\mathbf{k}\cdot\mathbf{p}$ method, described next.

III. THE k·p FOR BULK SOLIDS AND DOTS

The purposes of this section are to (i) describe the approximations underlying the standard $\mathbf{k}\cdot\mathbf{p}$ model as compared with the direct-diagonalization approach. This will provide guidance as to what may cause the errors in $\mathbf{k}\cdot\mathbf{p}$ performances. (ii) provide useful working equations for the $\mathbf{k}\cdot\mathbf{p}$ method.

A. 8×8 k·p for bulk periodic solids: Plane-wave representation

Since the $\mathbf{k}=0$ (zone-center) Bloch functions $\{u_{n,\mathbf{k}=0}\}$ of Eq. (3) form a complete function set, one can expand the wave function as

$$\psi(\mathbf{r})=\sum_{m=1}^{N_b}\left[\sum_{\mathbf{k}} b_m(\mathbf{k})e^{i\mathbf{k}\cdot\mathbf{r}}\right]u_{m,\mathbf{k}=0}(\mathbf{r})$$

$$=\sum_{m=1}^{N_b} F_m(\mathbf{r})u_{m,\mathbf{k}=0}(\mathbf{r}), \tag{6}$$

where $F_m(\mathbf{r})$ is the ''envelope function.'' Inserting Eq. (6) into Eq. (1) gives

$$\sum_{m=1}^{N_b}\left[\left(\epsilon_{n,0}+\frac{\hbar^2k^2}{2m_0}-\epsilon_{n,\mathbf{k}}\right)\delta_{m,n}+\frac{\hbar}{m_0}\,\mathbf{k}\cdot\mathbf{P}_{n,m}\right]b_m(\mathbf{k})=0, \tag{7}$$

where $\mathbf{P}_{n,m}=\langle u_{n,0}(\mathbf{r})|-i\hbar\nabla|u_{m,0}(\mathbf{r})\rangle$ is the momentum matrix element, $\epsilon_{n,0}$ is the band energy at $\mathbf{k}=0$. We see from Eq. (7) that (a) the deviation of $\epsilon_{n,\mathbf{k}}$ from the parabolic dispersion law originates in the $(\mathbf{k}\cdot\mathbf{P}_{n,m})$ term; (b) the information encoded in the microscopic potential $V(\mathbf{r})$ in Eq. (1) has now been transformed in Eq. (7) to $\{\epsilon_{n,0}\}$ and $\{\mathbf{P}_{n,m}\}$; and (c) given $\{\epsilon_{n,0}\}$ and $\{\mathbf{P}_{n,m}\}$ for a *converged basis*, Eq. (7) produces the bulk dispersion $\epsilon_{n,\mathbf{k}}^{\mathbf{k}\cdot\mathbf{p}}$ equivalent to $\epsilon_{n,\mathbf{k}}$ obtained via direct diagonalization of Eq. (1).

However, it is customary in $\mathbf{k}\cdot\mathbf{p}$ applications to severely truncate the number of bands N_b used. One often uses a single bulk conduction state at Γ (u_s) and three VBM states (u_x, u_y, and u_z). Including spin, this gives an ''8×8 model.'' If only the valence states are retained, we have a ''6×6 model,'' which includes, like the 8×8 model, the split-off band in the basis (although the numerical value of spin-orbit splitting Δ_0 is optional: $\Delta_0=0$ or $\Delta_0\neq0$). The neglect of the split-off valence band leads to a ''4×4 model.'' As the bases are truncated, one expects to find in the bulk $\mathbf{k}\cdot\mathbf{p}$ approach of Eq. (7) some errors[22–26] in the predicted dispersion relation $\epsilon_{n,\mathbf{k}}^{\mathbf{k}\cdot\mathbf{p}}$. The convergence of $\epsilon_{n,\mathbf{k}}^{\mathbf{k}\cdot\mathbf{p}}$ with N_b was examined previously[24] in a ''first-principles $\mathbf{k}\cdot\mathbf{p}$ approach''. In this approach, Eqs. (1)–(4) were first solved for bulk GaAs via a direct-diagonalization approach, thus producing the ''exact'' dispersion $\epsilon_{n,\mathbf{k}}$ as well as the input $\{\epsilon_{n,0},\mathbf{P}_{n,m}\}$ needed in $\mathbf{k}\cdot\mathbf{p}$ calculations. Using this input, the $\mathbf{k}\cdot\mathbf{p}$ equation (7) was then solved for different basis sizes N_b. The resulting $\epsilon_{n,\mathbf{k}}^{\mathbf{k}\cdot\mathbf{p}}$ was then examined as a function of the number of bands N_b used, and compared with the ''exact'' dispersion $\epsilon_{n,\mathbf{k}}$. It was found that for the X_{1c} bulk state, for example, reducing the $\mathbf{k}\cdot\mathbf{p}$ error to 1 meV requires $N_b\sim150$ Γ-like Bloch bands, but if $N_b=10$ Γ-like bands were used, the error was as large as 300 meV. If N_b was further reduced to 8, the error in X_{1c} went up to 20 eV, and the curvatures (hence, effective masses) of the valence bands have a negative sign. Application of direct-diagonalization and ''first-principles $\mathbf{k}\cdot\mathbf{p}$'' to GaAs/AlAs superlattices[23] showed that the errors vs N_b parallel those in bulk GaAs.

The problem of the inadequacy of a small basis set $\mathbf{k}\cdot\mathbf{p}$ to reproduce bulk dispersion away Γ can be solved in part by treating $\{\mathbf{P}_{n,m}\}$ as adjustable parameters and introducing into the Hamiltonian new terms that are allowed by symmetry and can be empirically adjusted. The new terms and their adjustable parameters are justified *pro forma* by viewing them as a consequence of ''folding-in'' of states outside the explicit bases (Löwdin folding[37]). Using the explicit bases of $\{u_s^\uparrow,u_x^\uparrow,u_y^\uparrow,u_z^\uparrow,u_s^\downarrow,u_x^\downarrow,u_y^\downarrow,u_z^\downarrow\}$ in Eq. (7) and perturbation theory,[38] one has the 8×8 $\mathbf{k}\cdot\mathbf{p}$ Hamiltonian matrix as

$$H_{8\times8}(\mathbf{k})=\begin{pmatrix} H_{\rm nso}(\mathbf{k})+Q_{\rm so} & R_{\rm so} \\ -R_{\rm so}^* & H_{\rm nso}^*(\mathbf{k})+Q_{\rm so}^*\end{pmatrix}, \tag{8}$$

where

$$H_{\rm nso}(\mathbf{k})=\begin{bmatrix} \epsilon_{c,0}+A'k^2 & iPk_x+B'k_yk_z & iPk_y+B'k_xk_z & iPk_z+B'k_xk_y \\ -iPk_x+B'k_yk_z & Ak_x^2+B(k_y^2+k_z^2) & Ck_xk_y & Ck_xk_z \\ -iPk_y+B'k_xk_z & Ck_xk_y & Ak_y^2+B(k_x^2+k_z^2) & Ck_yk_z \\ -iPk_z+B'k_xk_y & Ck_xk_z & Ck_yk_z & Ak_z^2+B(k_x^2+k_y^2) \end{bmatrix}, \tag{9}$$

$$Q_{\rm so}=\frac{\Delta_0}{3}\begin{pmatrix} 0 & 0 & 0 & 0 \\ 0 & 0 & -i & 0 \\ 0 & i & 0 & 0 \\ 0 & 0 & 0 & 0 \end{pmatrix}, \quad R_{\rm so}=\frac{\Delta_0}{3}\begin{pmatrix} 0 & 0 & 0 & 0 \\ 0 & 0 & 0 & 1 \\ 0 & 0 & 0 & -i \\ 0 & -1 & i & 0 \end{pmatrix}, \tag{10}$$

where $k^2=k_x^2+k_y^2+k_z^2$, Δ_0 is the energy splitting due to spin-orbit interaction, and A', B', A, B, and C are the symmetry-allowed adjustable parameters[38] of the second-order perturbation matrix elements due to the operator $(\mathbf{k}\cdot\mathbf{P}_{n,m})$ in Eq. (7). $P=-i\hbar/m_o\langle u_s|P_x|u_x\rangle$ describes the coupling between conduction and valence bands.

The Löwdin folding modifies the elements of the Hamiltonian matrix from the ''first principles $\mathbf{k}\cdot\mathbf{p}$'' scheme to new elements $\{A,B,C,A',B',P\}$ in Eq. (9) so that the eigenvalues of the $N_b\times N_b$ submatrix spanned by the N_b energy states equal the eigenvalues of the original, full matrix. The general procedure is to adjust the $\mathbf{k}\cdot\mathbf{p}$ parameters of Eq. (8) so that the curvatures of the solution $e_{n\mathbf{k}}^{\mathbf{k}\cdot\mathbf{p}}$ fit the experimentally measured *bulk* effective masses. In the diamond lattice B' vanishes by symmetry, but this condition is also often applied[39] to zincblende and wurzite structures without inversion symmetry. Also, A' is often used to fit the electron effective mass. The parameters $\{A,B,C\}$ of Eq. (9) are often discussed in terms of the Luttinger parameters,

$$\gamma_1=-\tfrac{2}{3}(A+2B), \quad \gamma_2=-\tfrac{1}{3}(A-B), \quad \gamma_3=-\tfrac{1}{3}C. \tag{11}$$

For the bulk material, the relationships between the parameters $\{\gamma_1,\gamma_2,\gamma_3\}$ and the effective masses are described as in the Appendix of Ref. 23. It is important to notice that the fitting of effective masses applies to the 3D-periodic bulk solids. Therefore, the use of the ensuing parameters to describe other systems (e.g., 0D quantum dots) is not protected by the underlying formalism.

Instead of the basis set $\{u_s^\uparrow,u_x^\uparrow,u_y^\uparrow,u_z^\uparrow,u_s^\downarrow,u_x^\downarrow,u_y^\downarrow,u_z^\downarrow\}$, for the consideration of symmetry (also for the later use in quantum dots), one can also use another set of Bloch basis $|J,J_z\rangle$, specified by the angular momentum $\mathbf{J}=\mathbf{L}_B+\mathbf{S}$ and its z component J_z. Here, $\mathbf{L}_B$ is the angular momentum of *Bloch* orbit, and $\mathbf{S}$ is the spin. The bases $|J,J_z\rangle$ are defined as

$$|\tfrac{1}{2},\tfrac{1}{2}\rangle_e=u_s|\uparrow\rangle,$$

$$|\tfrac{1}{2},-\tfrac{1}{2}\rangle_e=u_s|\downarrow\rangle,$$

$$|\tfrac{3}{2},\tfrac{3}{2}\rangle_h=u_+|\uparrow\rangle,$$

$$|\tfrac{3}{2},\tfrac{1}{2}\rangle_h=\frac{1}{\sqrt{3}}(-u_+|\downarrow\rangle+\sqrt{2}u_z|\uparrow\rangle),$$

$$|\tfrac{3}{2},-\tfrac{1}{2}\rangle_h=\frac{1}{\sqrt{3}}(u_-|\uparrow\rangle+\sqrt{2}u_z|\downarrow\rangle),$$

$$|\tfrac{3}{2},-\tfrac{3}{2}\rangle_h=u_-|\downarrow\rangle,$$

$$|\tfrac{1}{2},\tfrac{1}{2}\rangle_h=\frac{1}{\sqrt{3}}(\sqrt{2}u_+|\downarrow\rangle+u_z|\uparrow\rangle),$$

$$|\tfrac{1}{2},-\tfrac{1}{2}\rangle_h=\frac{1}{\sqrt{3}}(-\sqrt{2}u_-|\uparrow\rangle+u_z|\downarrow\rangle), \tag{12}$$

where $u_+=1/\sqrt{2}(u_x+iu_y)$ and $u_-=1/\sqrt{2}(u_x-iu_y)$. The corresponding Hamiltonian matrix in the basis set of Eq. (12) corresponds to a unitary transform of the matrix in Eq. (8), and is given in Appendix A.

B. 8×8 k·p for bulk and dots: spherical-wave representation

The application of $\mathbf{k}\cdot\mathbf{p}$ method to quantum dots involves[40] replacing the k_x, k_y, and k_z in Hamiltonian matrix elements in Eq. (A2) (see Appendix A) by the operators $-i\partial/\partial x$, $-i\partial/\partial y$, and $-i\partial/\partial z$, and expanding the envelope function $F_m(\mathbf{r})$ in Eq. (6) by plane waves. This was used extensively for quantum wells.[39] However, for spherical quantum dots, this approach is computationally ineffective, a more convenient approach[19] is to expand the plane-wave-like envelope function $e^{i\mathbf{k}\cdot\mathbf{r}}$ in Eq. (6) by spherical waves $|k,L,L_z\rangle\equiv\sqrt{2/\pi}h_L(kr)Y_{L,L_z}(\theta,\phi)$ [where $h_L(kr)$ is the spherical Hankel function, and Y_{L,L_z} is the spherical harmonic function] via the relationship

$$e^{i\mathbf{k}\cdot\mathbf{r}}=\frac{1}{\sqrt{(2\pi)^3}}\sum_{L,L_z}Y_{L,L_z}^*(\hat{\mathbf{k}})|k,L,L_z\rangle, \tag{13}$$

where $\hat{\mathbf{k}}$ is the angular direction vector of $\mathbf{k}$. By using Eqs. (12) and (13), the total bulk wave function in Eq. (6) then becomes

$$\psi(\mathbf{r})=\sum_{L,L_z}\sum_{J,J_z}\sum_{\mathbf{k}}\tilde{b}_{L,L_z,J,J_z}(\mathbf{k})|k,L,L_z|J,J_z\rangle, \tag{14}$$

where $\tilde{b}_{L,L_z,J,J_z}(\mathbf{k})$ are the wave function expansion coefficients. $|J,J_z\rangle$ and $|k,L,L_z\rangle$ are, respectively, the Bloch component [related with different *bulk* bands via Eq. (12)] and the spherical envelope component [related with usual plane-wave-like bulk envelope function $e^{i\mathbf{k}\cdot\mathbf{r}}$ via Eq. (13)].

An almost universally adopted approximation[2,7,15,16,19] in the application of $\mathbf{k}\cdot\mathbf{p}$ to quantum dots is to take $A=B+C$ in Eq. (8) [i.e., $\gamma_2=\gamma_3$ in Eq. (11)]. Under this *isotropic band* approximation, the bulk band dispersion depends only on the amplitude of $\mathbf{k}$, and the total momentum operator $\mathbf{F}=\mathbf{L}+\mathbf{J}$ is a conserved quantity.[41] Thus, the Hamiltonian matrix elements between different $\{F,F_z\}$ vanish. By the theory of angular momentum coupling[42] [i.e., linearly combining the bases $|k,L,L_z\rangle|J,J_z\rangle$ in Eq. (14)], the new bases of the irreducible representation of ensemble quantities $\{F,F_z,J,L\}$ can be written as

$$|F,F_z,J,L\rangle=\sum_{L_z}\sum_{J_z}\lambda^{F,F_z}_{L,L_z,J,J_z}|k,L,L_z\rangle|J,J_z\rangle, \quad (15)$$

where $\lambda^{F,F_z}_{L,L_z,J,J_z}$ is the Clebsch-Gorden coefficient.[42] Combining Eqs. (A1), (13), and (15), the block-diagonal Hamiltonian matrix in the bases $|F,F_z,J,L\rangle$ can be obtained. The explicit expressions for the Hamiltonian blocks corresponding to $F=\frac{1}{2}$ and $F=\frac{3}{2}$ are given in Eqs. (B1)–(B3) in Appendix B. These equations will be used in the electronic structure of both bulk and dots.

Equations (B1)–(B3) in Appendix B are basically an 8×8 $\mathbf{k}\cdot\mathbf{p}$ model except that they are cast in a spherical approximation. While this 8×8 model can be applied directly, almost all $\mathbf{k}\cdot\mathbf{p}$ studies on quantum dots use a simplified way: decouple first the conduction states from the valence states, thus, leading to a 6×6 model for the valence states and a 2×2 model for the conduction states. We will follow this practice too.

C. 6×6 $\mathbf{k}\cdot\mathbf{p}$: valence states

By diagonalizing the decoupled Hamiltonian submatrice for valence states [Eqs. (B1)–(B3) with $P=0$] for a given wave vector $\mathbf{k}$, we obtain, in each submatrix corresponding to the fixed good quantum numbers $\{F,F_z\}$, the isotropic *bulk* dispersion $\epsilon^{\rm iso}_{nk}$, and wave function

$$|\chi^{F,F_z}_{nk}(\mathbf{r})\rangle=\sum_{J,L}a^{(n)}_{J,L}\,|F,F_z,J,L\rangle$$

$$=\sum_{J,L}a^{(n)}_{J,L}\,h_L(kr)\,|F,F_z,J,L\rangle_{\theta,\phi}, \quad (16)$$

where we use the definition of spherical wave $|k,L,L_z\rangle$ to write out the radial part. The wave functions of Eq. (16) are ''bulk orientated'' in the sense that they come from bulk Hamiltonian except that they are calculated in terms of spherical waves. These wave functions do not satisfy the boundary condition of dots, where the wave functions are required to vanish at dot's boundary of infinite barrier. In order to satisfy the dot boundary condition and the intrinsic bulk dispersion relationship, the dot wave functions need to be a linear combination of all the solutions of Eq. (16) with the same energy $\epsilon^{\rm iso}_{nk}$, i.e.,

$$\psi^{\rm dot}(\mathbf{r})=\sum_n C_n|\chi_{nk}(\mathbf{r})\rangle=\sum_n\sum_{J,L}C_n a^{(n)}_{J,L}|F,F_z,J,L\rangle$$

$$=\sum_n\sum_{J,L}C_n a^{(n)}_{J,L}h_L(k_n r)|F,F_z,J,L\rangle_{\theta,\phi}, \quad (17)$$

where we use Eq. (16) in the derivation. The condition that the wave function vanishes at the boundary of the dot $r=R$ yields the determinant equation

$$det|a^{(n)}_{J,L}h_L(k_nR)|=0, \quad (18)$$

where k_n is an implicit function of energy by inverting the dispersion relation $\epsilon^{\rm iso}_{nk}$.

In our $\mathbf{k}\cdot\mathbf{p}$ implementation for quantum dots, (i) we invert the isotropic dispersion $\epsilon^{\rm iso}_{nk}$ [obtained via Eqs. (B1)–(B3) with $P=0$] for each irreducible representation $|F,F_z\rangle$ and a given energy ϵ, thus finding the wave vectors k_n [i.e., the ''inverse dispersion''] and the bulk-orientated wave-function coefficients $a^{(n)}_{J,L}$ [see Eq. (16)]; (ii) The boundary condition [Eq. (18)] is then used to find out whether the assumed energy ϵ is the dot energy level; (iii) Unlike the work of Sercel and Vahala[19] where only a 4×4 model is used for dot valence states (i.e., the split-off valence band is neglected), all the present $\mathbf{k}\cdot\mathbf{p}$ calculations are done by the 6×6 model; (iv) The whole procedure to find the energy levels of dots are realized numerically avoiding many analytic formulae that are quite complicated.

D. 2×2 $\mathbf{k}\cdot\mathbf{p}$: conduction states

For the conduction states, a 2×2 model is obtained after decoupling. The effect of interaction between valence bands and conduction bands is taken into account by a perturbation theory as described in Ref. 43. The resulting single Schrodinger equation for the electron is

$$\omega(\epsilon)\left(-\frac{\hbar^2}{2m_0}\right)\nabla^2\psi=(\epsilon-\epsilon_g)\psi, \quad (19)$$

where

$$\omega(\epsilon)=1+2f+\frac{2m_0P^2}{3\hbar^2}\left(\frac{2}{\epsilon}+\frac{1}{\epsilon+\Delta}\right). \quad (20)$$

The parameter $f=(A'-1)/2$ is used to fit the electron effective mass. Our calculated conduction band energies for bulk use Eq. (19). In *quantum dots*, Eq. (19) can be solved either with infinite barrier or finite barrier. Assuming a finite barrier ΔE_c for electron outside dots, and imposing the continuities of dot wave function and its derivative, the energy levels for dot conduction states can be calculated by

$$\omega(\epsilon)k_d\frac{j'_L(k_dR)}{j_L(k_dR)}=ik_b\frac{h'_L(ik_bR)}{h_L(ik_bR)}, \quad (21)$$

where j_L is the spherical Bessel function, and

$$k_d = \sqrt{\frac{2m_0}{\hbar^2}\frac{\epsilon-\epsilon_g}{\omega(\epsilon)}},$$

$$k_b = \sqrt{\frac{2m_0}{\hbar^2}(-\epsilon+\epsilon_g+\Delta E_c)} \tag{22}$$

are the wave vectors in the dot and in the barrier, respectively.

E. Summary of k·p approximations

The $\mathbf{k}\cdot\mathbf{p}$ approximations for quantum dots are:

(a) The truncation of the number of Γ-like Bloch bases, and the use of second-order perturbation to correct this. In practice, these approximations are mitigated by treating the $\mathbf{k}\cdot\mathbf{p}$ parameters as adjustable parameters fitted to the observed bulk effective masses. The extent to which these parameters work for systems other than fitted (e.g., nanometer dots) remains unknown.

(b) The valence states and conduction states are calculated in a decoupled way. The 8×8 model then breaks into 6×6 valence-only plus 2×2 conduction-only matrice.

(c) The isotropic approximation is used for the dot valence states (i.e., $\gamma_2=\gamma_3$), and then the dispersion $\epsilon_{n\mathbf{k}}^{\mathbf{k}\cdot\mathbf{p}}$ depends only on the amplitude of $\mathbf{k}$.

(d) The method does not consider the existence of real dot surface states or interface states at the dot's boundary.

IV. RESULTS AND DISCUSSIONS

InP and CdSe colloidal quantum dots were studied extensively both experimentally[1–7] and theoretically.[2,15,16] In particular, the observed photoluminescence spectra were interpreted by $\mathbf{k}\cdot\mathbf{p}$ models.[1–4,7,15,16] For CdSe dots, the $\mathbf{k}\cdot\mathbf{p}$ was also used to assign the observed high excited transitions,[2] however, the $\mathbf{k}\cdot\mathbf{p}$ parameters were adjusted to fit the experimental data of the *dot*.[2,4] For InP dots, the 6×6 $\mathbf{k}\cdot\mathbf{p}$ predicted that the lowest valence-to-conduction transition is dipole forbidden.[7,15] This was used to explain the carrier dynamics.[7] We are interested in these two materials for an additional reason, namely, that InP and CdSe have quite different magnitudes of spin-orbit splitting: $\Delta_0=0.11$ eV for InP and $\Delta_0=0.42$ eV for CdSe. Therefore, we can investigate how this difference will affect the applicability of $\mathbf{k}\cdot\mathbf{p}$ model to quantum dots.

For the purpose of a consistent comparison between the direct diagonalization [Eqs. (1) and (5)] and $\mathbf{k}\cdot\mathbf{p}$ model [Eqs. (16)–(22)], the $\mathbf{k}\cdot\mathbf{p}$ Luttinger parameters are all calculated from the curvature of the *bulk-material* dispersion obtained by direct diagonalization using the same pseudopotential employed in dot calculations. These screened atomic pseudopotentials[31,32] are derived from local-density-approximation (LDA) calculation, and are able to reproduce the LDA wave functions and the *experimentally observed* (not LDA) bulk transition energies, effective masses, deformation potentials. The kinetic energy cutoff in dot calculation is taken the same as in deriving the potential from bulk solids, i.e., 6.8 Ry for InP and 6.88 Ry for CdSe. The lattice constants for InP and CdSe are 5.83 Å and 6.08 Å, respectively. After the effective masses of zincblende bulk materials are calculated by the pseudopotential approach (see results in Table I), the Luttinger parameters $\{\gamma_1,\gamma_2,\gamma_3\}$ are obtained from Eqs. (B4) and (B5) in Appendix B. The average $\overline{\gamma_2}=(2\gamma_2+3\gamma_3)/5$ is used to replace the value of γ_2 in the isotropic $\mathbf{k}\cdot\mathbf{p}$ Hamiltonian.[44] Table I lists the pseudopotential effective masses and the ensuing $\mathbf{k}\cdot\mathbf{p}$ parameters used here for zinc-blende (ZB) InP and ZB CdSe. We see in Table I that for InP the effective masses calculated from the

TABLE I. The 6×6 $\mathbf{k}\cdot\mathbf{p}$ parameters of ZB InP and ZB CdSe used in this work: the band gap ϵ_g, $E_p=2m_0P^2/\hbar^2$, and the parameter f for conduction state [Eq. (20)]; the spin-orbit splitting Δ_0, the Luttinger parameters γ_1, γ_2, γ_3, and the averaged parameter $\overline{\gamma_2}$ for valence states. The calculated (pseudopotential) bulk effective masses, from which the Luttinger parameters γ_1, γ_2, and γ_3 are derived, are also listed in the table. For ZB InP, two sets of parameters corresponding to $\Delta_0=0$ and $\Delta_0\neq0$ are given, and the available experimental effective masses are also listed for comparison (in parentheses, column $\Delta_0\neq0$). ϵ_g, E_p, and Δ_0 are in units of eV.

Parameters	InP		CdSe
	$\Delta_0=0$	$\Delta_0\neq0$	
ϵ_g	1.45	1.42	1.84
E_p	20.0	20.0	17.4
f	−0.42	−0.42	−0.75
Δ_0	0.00	0.11	0.42
γ_1	4.86	4.94	2.52
γ_2	1.37	1.50	0.65
γ_3	1.85	1.99	0.95
$\overline{\gamma_2}$	1.66	1.79	0.83
m_e	0.072	0.072 (0.079[a])	0.119
$m_{hh}(001)$	0.474	0.513 (0.52[b], 0.61[c])	0.820
$m_{hh}(111)$	1.030	1.055 (0.95[d])	1.613
$m_{lh}(001)$	0.097	0.126 (0.10[c], 0.12[e])	0.262
$m_{lh}(111)$	0.083	0.112	0.226

[a]Reference 45.
[b]Reference 46.
[c]Reference 47.
[d]Reference 48.
[e]Reference 49.

TABLE II. Hole effective masses of wurzite bulk CdSe, calculated by our pseudopotential-derived $\gamma_1=2.52$, $\overline{\gamma_2}=0.83$, and the quasicubic model. The results are compared with two sets of experimental values. The experimental values in the third column are obtained by subtracting from the measured excitonic masses the electron mass. We also give the values obtained using $\gamma_1=2.04$, $\overline{\gamma_2}=0.58$ fitted by Norris and Bawendi (Ref. 2) to the measurements on CdSe dots.

Masses	Ref. 2	Present work	Expt.	
			Hermann and Yu[a]	Bir and Pikus[b]
$m_{\parallel}^A$	1.14	1.16	1.19	>1
$m_{\perp}^A$	0.38	0.30	0.29	0.45±0.09
$m_{\parallel}^B$	0.31	0.24		
$m_{\perp}^B$	0.68	0.60		0.9±0.2

[a]Reference 51.
[b]Reference 52.

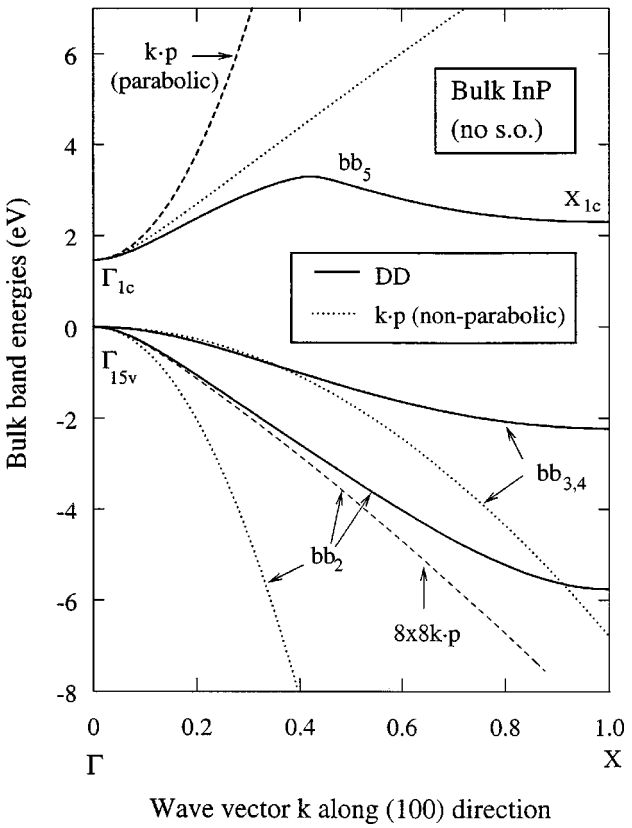

FIG. 2. Band dispersions of bulk InP along the ΓX direction as calculated by pseudopotential direct diagonalization (DD, solid lines) and by the 6×6 (for valence) and 2×2 (for conduction) $\mathbf{k}\cdot\mathbf{p}$ model (dotted lines). For the conduction band, the single-band parabolic $\mathbf{k}\cdot\mathbf{p}$ dispersion is shown in thick dashed line. For the light-hole band, in addition to the 6×6 $\mathbf{k}\cdot\mathbf{p}$ (with $\gamma_1=4.86$, $\overline{\gamma_2}=1.66$, $\Delta_0=0$) dispersion (dotted line), the 8×8 $\mathbf{k}\cdot\mathbf{p}$ (with $\gamma_1'=1.42$, $\overline{\gamma_2'}=-0.062$, $E_p=14.98$, $\alpha=1.0$) dispersion is also shown in thin dashed line. The notation bb_n ($n=2$ to 5) indicates the 2nd to 5th bulk bands in the order of increasing energy. All curves are calculated with the spin-orbit parameter $\Delta_0=0$.

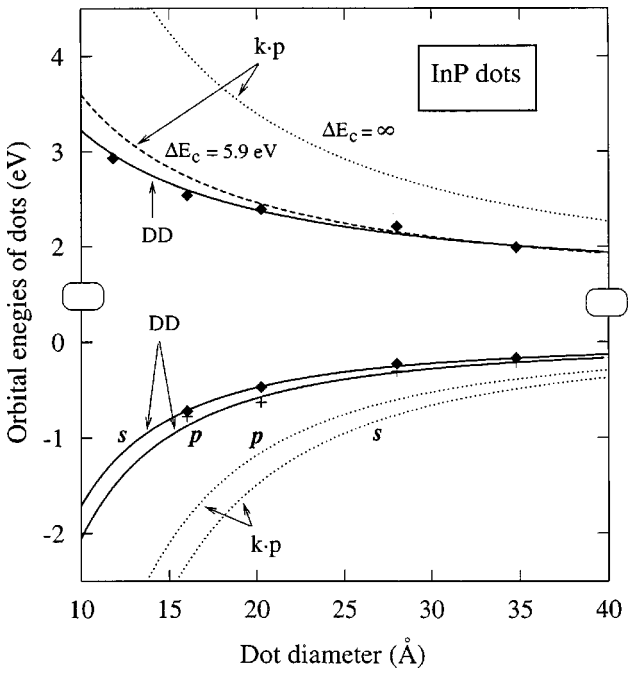

FIG. 3. The orbital energies of the lowest conduction state and of the two highest valence states of InP dots. Diamond and cross symbols correspond to s- and p-like levels calculated by direct diagonalization (DD), and solid lines are guides for eyes. Dotted lines give results of $\mathbf{k}\cdot\mathbf{p}$ model. For the dot conduction state in the $\mathbf{k}\cdot\mathbf{p}$ model, we show results calculated both with an infinite barrier (dotted line) and with a finite barrier (dashed line).

pseudopotential theory agree well with experiments.[45–49] Since CdSe exists experimentally in the wurzite (WZ) form, we can assess the quality of our parameters by converting our ZB results to WZ results. We use our pseudopotential-derived γ_1 and $\overline{\gamma_2}$ from the zinc-blende structure (Table I) and compute the effective masses of wurzite CdSe using the quasicubic model[50] (i.e., $1/m_{\parallel}^{A}=\gamma_1-2\overline{\gamma_2}$, $1/m_{\perp}^{A}=\gamma_1+\overline{\gamma_2}$). The calculated masses of wurzite CdSe are compared in Table II with experimental values[51,52] and with the values using $\gamma_1=2.04$ and $\overline{\gamma_2}=0.58$ fitted by Norris and Bawendi[2] to the measurements on CdSe dots. We see that our CdSe Luttinger parameters give effective masses close to experimental values.

Since the spin-orbit splitting Δ_0 is quite small for InP, for the simplicity of computation, Δ_0 will be taken as zero both in the direct diagonalization and in the $\mathbf{k}\cdot\mathbf{p}$ calculations. We compared the theoretical results of InP quantum dots with $\Delta_0=0$ and those with $\Delta_0=0.11$ eV (our pseudopotential value), and found that the energy levels and the wave functions of the dots change but slightly.

A. InP bulk band structures

Figure 2 compares the InP bulk band structure obtained using the $\mathbf{k}\cdot\mathbf{p}$ model [Eq. (19) and Eqs. (B1)–(B3)] with the exact, pseudopotential direct diagonalization result [Eq. (1)]. Here, we label the bulk bands (bb) with a band index n in the increasing order of energy (without counting spin degeneracy). The lowest conduction band (bb_5) was calculated by using the 2×2 $\mathbf{k}\cdot\mathbf{p}$ approach with both parabolic dispersion ($\hbar^2k^2/2m^*$) and the nonparabolic Schrodinger equation [Eq. (19)]. We see that

(i) Including the nonparabolic effect in the conduction band (bb_5) improves considerably the $\mathbf{k}\cdot\mathbf{p}$ dispersion near Γ. However, a large deviation still remains near the X point.

(ii) The $\mathbf{k}\cdot\mathbf{p}$ dispersion of the heavy-hole-like valence bands ($bb_{3,4}$) agrees well with the direct-diagonalization result near the zone center, but this agreement becomes unsatisfactory near X.

(iii) For the light-hole band (bb_2), the whole band calculated by the 6×6 $\mathbf{k}\cdot\mathbf{p}$ model differs significantly from the direct-diagonalization result.

B. InP quantum dots: Energy levels and wave functions

We consider five spherical dots $In_{19}P_{16}$, $In_{44}P_{43}$, $In_{92}P_{83}$, $In_{240}P_{225}$, and $In_{456}P_{435}$ with diameters D of 11.8, 16.0, 20.2, 28.0, and 34.8 Å, respectively. The dot surfaces were fully passivated.[21] Figure 3 compares the orbital energies of the lowest conduction state and the two highest valence states of InP dots, calculated by the $\mathbf{k}\cdot\mathbf{p}$ method [using Eqs. (16)–(18) for valence states and Eqs. (19)–(22) for conduction states] and by the direct-diagonalization method. In order to parallel the $\mathbf{k}\cdot\mathbf{p}$ studies in the literatures, we use in the $\mathbf{k}\cdot\mathbf{p}$ calculations the 6×6 model with infinite barrier for the

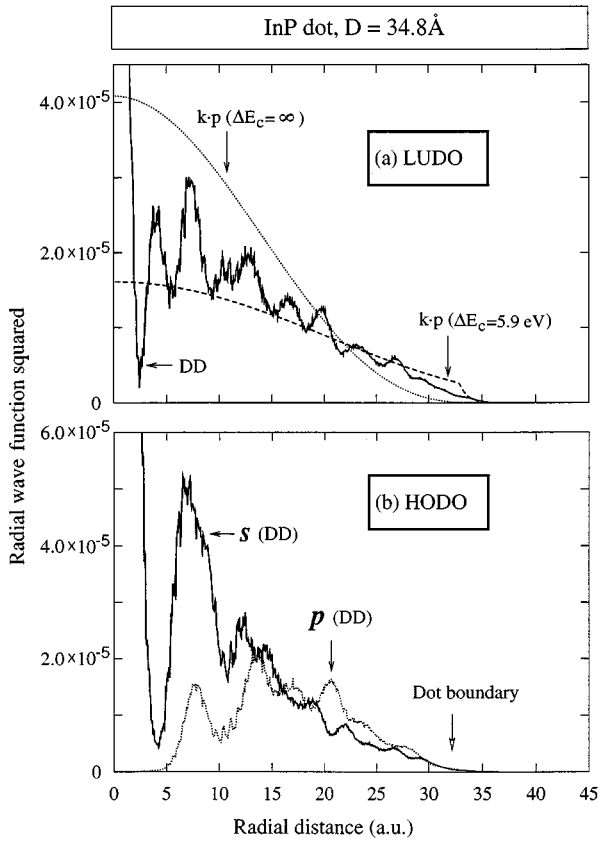

FIG. 4. Radial wavefunctions squared of the 34.8 Å diameter InP dot as obtained in direct diagonalization (DD, solid lines): (a) the lowest unoccupied dot orbit (LUDO); (b) two highest dot occupied orbits (HODO's) with s and p symmetries. For the LUDO, the $\mathbf{k}\cdot\mathbf{p}$ radial wave functions squared of finite and infinite barriers are also shown in dashed and dotted lines, respectively.

dot valence states, while a 2×2 model with both infinite and finite barriers is used for the dot conduction states. The finite barrier height is taken to be the work function of InP material ($\Delta E_c = 5.9$ eV).

1. Conduction states of InP dots

The $\mathbf{k}\cdot\mathbf{p}$ prediction for the lowest conduction state using infinite barrier significantly overestimates the *electron* confinement energy compared with the exact direct diagonalization. Using a finite barrier reduces the confinement energy, in closer agreement with the results of direct diagonalization. Fitting the energies of the lowest conduction states of different size dots gives ($\epsilon_c^{\rm dot}$ in units of eV relative to the bulk VBM energy, D in units of Å)

$$\epsilon_c^{\rm dot}=\begin{cases}1.45+15.10/D^{0.93} & \text{(direct diagonalization)};\\ 1.45+84.52/D^{1.26} & (\mathbf{k}\cdot\mathbf{p}\text{ with infinite barrier});\\ 1.45+26.25/D^{1.09} & (\mathbf{k}\cdot\mathbf{p}\text{ with finite barrier}).\end{cases} \tag{23}$$

Figure 4(a) shows the radial wave function squared $\int|\psi(\mathbf{r})|^2 d\theta d\phi$ of the lowest dot conduction state as obtained from $\mathbf{k}\cdot\mathbf{p}$ model either with infinite (dotted line) or with finite (dashed line) barriers. It can be seen that the $\mathbf{k}\cdot\mathbf{p}$ wave function corresponding to infinite barrier is strongly ''confined,'' i.e., it decreases abruptly from the dot's center to the dot's boundary. However, the wave function computed with a finite barrier exhibits a kink at the dot's boundary. This reflects the requirement of current conservation and mass discontinuity. Furthermore, the wave function is rather flat inside the dot (implying a much weaker confinement). In contrast, the radial wave function squared obtained by direct diagonalization is intermediate in terms of confinement, and smoothly decays into the vacuum without any unphysical kink. The large amplitude (which is the quantity plotted in Fig. 4 multiplied by radius squared) of finite-barrier $\mathbf{k}\cdot\mathbf{p}$ wave function near the dot's boundary may cause incorrect electron-hole wave-function overlap, hence, incorrect Coulomb and exchange interactions.

2. Valence states of InP dots

The direct-diagonalization approach predicts for the valence states of InP dots that the HODO has a mostly s-like envelope function symmetry, and the next state below has a mostly p-like envelope function symmetry (Fig. 3). Note that the notation for the envelope here reflects only the majority angular character. The HODO has also p,d character, and thus is parity-mixed. Both states are threefold degenerate when $\Delta_0=0$, and twofold degenerate when $\Delta_0\neq0$. The symmetries can be gleaned from Fig. 4(b) that illustrates the radial wave function squared as obtained by the pseudopotential calculation. The radial wave function of the HODO has nonzero value at the origin (the dot's center), and the envelope can be described by spherical Bessel function $j_{L=0}(\alpha r)$, thus being s-like. In contrast, the next valence state below the HODO has a zero amplitude at the origin, and its envelope can be described by $j_{L=1}(\alpha r)$, thus being p-like. We find that, when we change the surface passivation potential (to simulate different ligands in experiments), the order of these s and p valence levels does not change. This reflects the fact that the wave-function amplitudes at the dot surface are very small [see Fig. 4(b)].

One may wonder whether the electron-hole Coulomb energy, which is different for s-like and for p-like hole states, can reverse the s/p order. We calculate the Coulomb energy, and find that, for the $D=34.8$ Å dot, the Coulomb energy of s-like hole with s-like electron is about 10 meV *larger* than that of p-like hole. Therefore, the inclusion of Coulomb interaction will not alter the s-above-p conclusion obtained in our direct diagonalization.

In contrast with the result of the direct diagonalization, the $\mathbf{k}\cdot\mathbf{p}$ model gives the opposite order of valence level, i.e., the HODO is p-like and the next state below is s-like (Fig. 3). One may ask at what dot size the s/p order in $\mathbf{k}\cdot\mathbf{p}$ will become correct. Our calculation shows that the $\mathbf{k}\cdot\mathbf{p}$-predicted p-above-s level order is not changed even for dot size as large as 250 Å diameter, where the energy difference of s- and p-like states is negligible (0.3 meV). This indicates that $\mathbf{k}\cdot\mathbf{p}$ gives the incorrect s/p level order all the dot sizes. This p-above-s order was also found in previous $\mathbf{k}\cdot\mathbf{p}$ calculations.[7,15]

Based on the fact that the p-like valence state is dipole forbidden to the s-like conduction state, the $\mathbf{k}\cdot\mathbf{p}$-predicted level sequence seems to be a natural explanation for the experimentally observed photoluminescence red shift[6] relative to the absorption in selective excitation. This reverse level

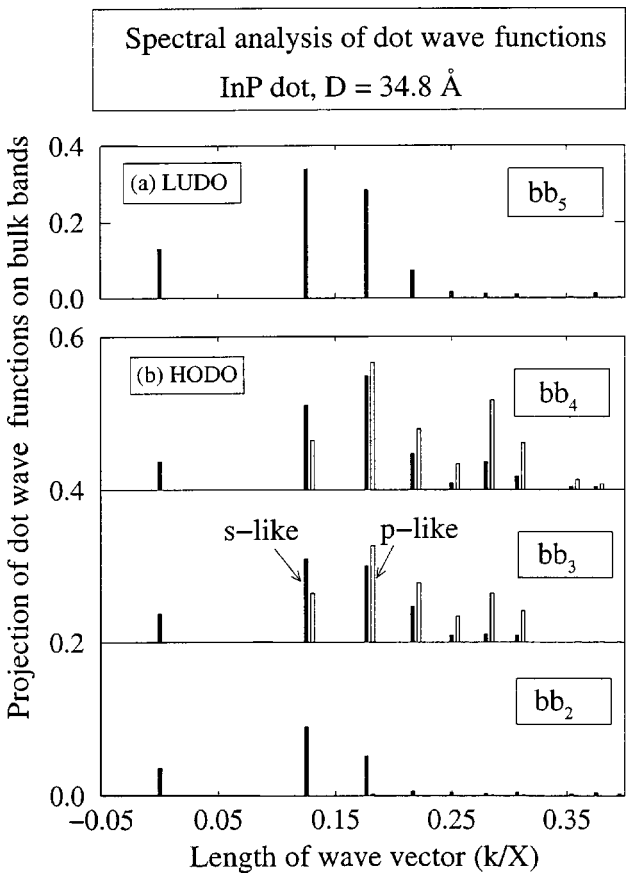

FIG. 5. Projection amplitude $|A_i(n\mathbf{k})|^2$ [see Eq. (25)] showing how much the bulk states $|n\mathbf{k}\rangle$ participate in forming the following states $|i\rangle$ of InP dot with 34.8 Å diameter: (a) the lowest unoccupied dot orbit (LUDO); (b) two highest occupied dot orbits (HODO's) with s-like symmetry (filled bars) and p-like symmetry (unfilled bars), where the unfilled bars are slightly shifted horizontally and the projections from different bulk bands to the HODO's are shifted vertically for clarity of display. The bulk bands bb_n are denoted by an index n in the increasing order of energy.

ordering obtained by $\mathbf{k}\cdot\mathbf{p}$ has been used to explain the carrier dynamical process involving a transition-forbidden lowest exciton state.[7] Unfortunately, our more accurate pseudopotential calculation shows that these explanations are not applicable, and other possibilities have to be sought.[21] Using $\mathbf{k}\cdot\mathbf{p}$-predicted energy-level scheme, the resonant red shift will be the single-particle energy difference of s- and p-like valence levels plus the exchange splitting. This will give the red shift of $\sim$100 meV, which is significantly larger than experimental measurements[6] (around 20 meV) for the $D=34.8$ Å dot.

As shown in Fig. 3, the energies obtained by the $\mathbf{k}\cdot\mathbf{p}$ calculation are significantly deeper than the direct diagonalization results, implying larger confinement. The difference is about 600 meV for the $D=20$ Å dot. Analytic fitting of the orbital energies of the dot valence states produces (relative to the bulk VBM energy)

$$\epsilon_v^{\rm dot}[s]=\begin{cases}-119.08/D^{1.84} & \text{(direct diagonalization)}\\ -595.52/D^2 & (\mathbf{k}\cdot\mathbf{p});\end{cases}$$

$$\epsilon_v^{\rm dot}[p]=\begin{cases}-130.93/D^{1.81} & \text{(direct diagonalization)};\\ -472.6/D^2 & (\mathbf{k}\cdot\mathbf{p}).\end{cases} \tag{24}$$

C. How do the errors in the bulk band structure propagate to the dot's electronic structure?

We would like to inquire how the electronic structure of the *bulk* (Sec. IV A) affects the energy levels of *dots* (Sec. IV B). In order to answer this question, we project each *dot* wave function $\psi_i^{\rm dot}$ [Eq. (5)] onto a set of wave functions of the *bulk* material $\psi_{n\mathbf{k}}^{\rm bulk}$ [Eq. (3)], i.e.,

$$\psi_i^{\rm dot}(\mathbf{r})=\sum_{n,\mathbf{k}} A_i(n\mathbf{k})\,\psi_{n\mathbf{k}}^{\rm bulk}, \tag{25}$$

where $\psi_i^{\rm dot}(\mathbf{r})$ and $\psi_{n\mathbf{k}}^{\rm bulk}$ are both calculated by the direct-diagonalization method, and $A_i(n\mathbf{k})$ are the spectral projection coefficients. The contribution to the dot state from a given bulk band is obtained as a sum over all the $\mathbf{k}$ points for this specific band, i.e.,

$$\widetilde{A}_i(n)=\sum_{\mathbf{k}} |A_i(n\mathbf{k})|^2. \tag{26}$$

Table III gives the band contribution $\widetilde{A}_i(n)$ to the dot near-edge states from the eight lowest bulk bands (not counting spin). Figure 5 depicts $|A_i(n\mathbf{k})|^2$ [Eq. (25)] as a function of the wave-vector length $\mathbf{k}$ for the dot $In_{456}P_{435}$ with diameter 34.8 Å. The projection [Eq. (25)] is implemented using a dot supercell that is commensurate with a cubic bulk cell [so only some discrete $\mathbf{k}$ points contribute to Eq. (25)]. If a noncommensurate dot supercell is used, the effect is just to broaden each peak in Fig. 5. The bulk wave function $\psi_{n\mathbf{k}}^{\rm bulk}$ in Eq. (25) is normalized in the dot supercell. This gives normalized projection contributions $A_i(n\mathbf{k})$.

1. Conduction states of InP dots

Considering the LUDO, we see that the contribution (throughout the Brillouin zone) from the lowest bulk conduction band bb_5 (85% to 92%, see Table III) dominates, indicating that a single bulk band (i.e., a 2×2 model) is quite adequate to describe the dot lowest conduction state.

Figure 5(a) shows however that the LUDO contains significant projection amplitude $|A_i(n\mathbf{k})|^2$ from off-Γ $\mathbf{k}$ points. With decreasing dot size, those $\mathbf{k}$ points contributing heavily will move further away from Γ point, so the $\mathbf{k}\cdot\mathbf{p}$ approach becomes worse. We thus conclude that the significant errors that $\mathbf{k}\cdot\mathbf{p}$ makes in describing the dispersion of the *bulk* conduction band (Fig. 2) will be transferred to the description of the conduction states of quantum dots.

Our direct diagonalization also predicts that for small InP dots, the next conduction state above the LUDO is not a Γ_{1c}-derived direct state as depicted by $\mathbf{k}\cdot\mathbf{p}$, but a L_{1c}-derived indirect state. To see that, we calculate the contribution $Q_i(\mathbf{k})=\Sigma_{n=1}^{\infty}|A_i(n\mathbf{k})|^2$ from the $\mathbf{k}$ points in the BZ. Figure 6 shows the projection amplitudes $Q_i(\mathbf{k})$ from the $\mathbf{k}$ points within the plane passing the Γ, X, L, K, and U points of the bulk Brillouin zone for the LUDO and the next state above the LUDO of $In_{92}P_{83}$ dot. The size of circle in this figure is proportional to the contribution from this $\mathbf{k}$ point. We see that the LUDO originates mainly from bulk states near the BZ center, thus being Γ_{1c}-derived, but the next dot state above the LUDO (''LUDO+1'') originates mainly from bulk states near the L point, thus being L_{1c} derived.

TABLE III. The contributions $\widetilde{A}_i(n)$ [Eq. (26)] of the InP bulk band with index n in forming the wave functions of InP quantum dots. The bulk bands are labeled from 1 to 8 in the order of increasing energy (see Fig. 2). LUDO and HODO mean the lowest unoccupied dot orbit and the highest occupied dot orbit, respectively.

Dot size	Bulk band	Projection on LUDO (%)	Projection on s-like HODO (%)	Projection on p-like HODO (%)
$In_{92}P_{83}$	1	0.33	0.23	0.28
($D=20.2$ Å)	2	3.47	20.45	0.89
	3+4	1.41	70.15	94.61
	5	84.37	3.75	1.13
	6+7+8	7.72	2.96	1.58
	all other	2.70	2.46	1.51
$In_{240}P_{225}$	1	0.14	0.19	0.15
($D=28.0$ Å)	2	2.50	21.86	0.98
	3+4	0.78	70.22	94.25
	5	90.22	2.94	0.84
	6+7+8	4.72	2.64	2.14
	all other	1.64	2.15	1.64
$In_{456}P_{435}$	1	0.13	0.15	0.12
($D=34.8$ Å)	2	2.67	20.75	0.55
	3+4	0.91	73.37	96.61
	5	91.55	2.38	0.67
	6+7+8	3.36	1.82	1.07
	all other	1.38	1.53	0.98

This L-derived indirect dot conduction state cannot be described by the usual $\mathbf{k}\cdot\mathbf{p}$ model.

2. Valence states of InP dots

Considering next the dot valence states, Table III and Fig. 5(b) show that

(i) the s-like dot valence state has a significant ($\sim$20%) contribution from bulk band bb_2 (i.e., light-hole band) whereas the p-like dot valence state has nearly no contribution from this bulk band. Since $\mathbf{k}\cdot\mathbf{p}$ overestimates the down-dispersion of bulk lh band (Fig. 2), it will also overestimate the confinement of the dot s-like valence state.

(ii) The contribution from the lowest bulk conduction band (bb_5) to the s-like dot state is larger than to the p-like dot state (see Table III). This suggests that the coupling between valence bands and conduction bands play a more important role for the s-like dot valence state than for the p-like dot valence state. We will show quantitatively (see Sec. IV D) that this kind of coupling is quite crucial in determining the s/p level order.

(iii) The s-like dot state has a significant amplitude at Γ point, while the p-like dot state has no amplitude at Γ (see Fig. 5). This suggests a way to distinguish the s-like dot state from the p-like dot state.

(iv) The $\mathbf{k}$ points contributing heavily to the p-like dot state are generally located further away from the zone center than those $\mathbf{k}$ points contributing heavily to the s-like dot state (see Fig. 5). Since $\mathbf{k}\cdot\mathbf{p}$ model can not describe well the far-off-Γ bulk dispersion, it will also introduce errors for the dot p-like states.

We next examine the above conclusions quantitatively.

D. Estimation of dot energy levels: The projection approach

Once the wave-function projection amplitudes $A_i(n\mathbf{k})$ [Eq. (25)] are available, we can estimate the *dot* energy levels by using the *bulk* band dispersion, i.e.,

$$\widetilde{\epsilon}_i^{\rm dot}=\sum_{n=1}^{M_b}\sum_{k}\epsilon_{n\mathbf{k}}^{\rm bulk}\,|A_i(n\mathbf{k})|^2, \tag{27}$$

where $\epsilon_{n\mathbf{k}}^{\rm bulk}$ is the bulk dispersion obtained either from pseudopotential calculation or from the $\mathbf{k}\cdot\mathbf{p}$ approach. In Eq. (27), we can intentionally change the number of bulk bands M_b [meanwhile, we need to normalize the amplitudes $A_i(n\mathbf{k})$] to investigate its effect on the dot energy level. Unlike the ''truncated crystal method'' [53] where only single band and single wavevector $\mathbf{k}$ are involved, our model of Eq. (27) involves multiband and multi-$\mathbf{k}$.

Table IV gives the energy levels of the LUDO state for three InP dots. Column 3 shows that when $M_b=8$ (not counting spin) pseudopotential bulk bands are used, the estimated energy levels using Eq. (27) agree very well with the direct-diagonalization result (column 2). Given that in the model of Eq. (27) surface effects are ignored, the agreement between the estimated and the directly calculated energy levels indicates that surface effects are small for the dot's LUDO state. This agreement remains even when we use only the lowest bulk conduction band in Eq. (27) (column 4 in Table IV) because of the dominant contribution from this bulk band. However, if we use in Eq. (27) the bulk dispersion given by the $\mathbf{k}\cdot\mathbf{p}$ model, the estimated energy levels of dot (column 5) become significantly worse than the direct pseudopotential result. We concluded that the LUDO can be

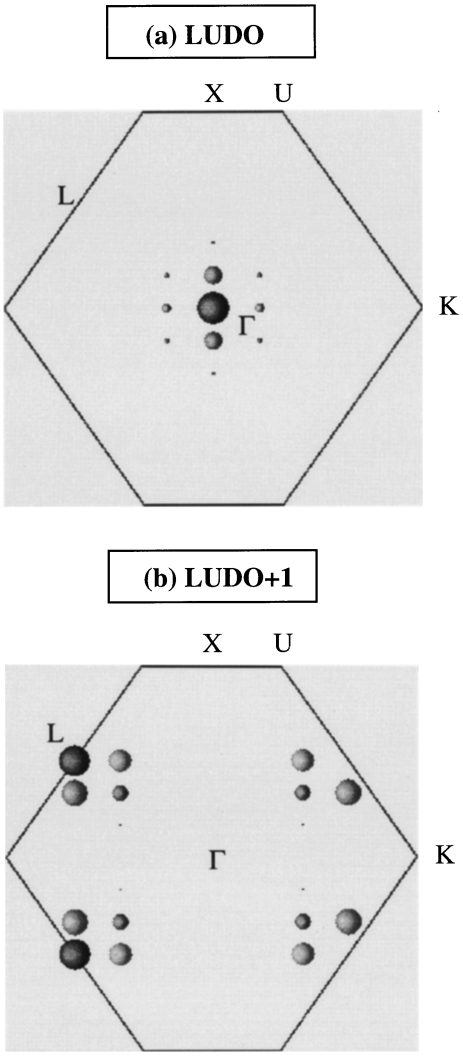

FIG. 6. The projection contribution $Q_i(\mathbf{k})=\Sigma_{n=1}^{\infty}|A_i(n\mathbf{k})|^2$ from those **k** points within the plane passing the Γ, *X*, *L*, *K*, and *U* points of the zincblende Brillouin zone in forming the two following conduction states of $In_{92}P_{83}$ dot with 20.2 Å diameter: (a) the LUDO; (b) the next unoccupied dot orbit above the LUDO (i.e., LUDO+1). The larger the circle, the heavier the projection contribution. The lines in this figure indicate the boundary of Brillouin zone. *X* and *L* points are located in the middle of respective lines. Note that the LUDO is Γ-like, while the next state above is *L*-like.

approximated well by a single band if, and only if this is the exact bulk band. Otherwise, (viz. the **k·p**) many more bands are needed.

Table V shows analogous results to Table IV but for the dot's valence states (both *s*-like and *p*-like). Column 3 shows that when we use $M_b=8$ pseudopotential bulk bands, the estimated energy levels are quite close to the direct calculation (column 2), and the HODO state is *s*-like. However, when we use only the three highest bulk valence bands in Eq. (27), the order of *s* and *p* levels changes, and the estimated energies (column 4) are now significantly different from the direct result (column 2), especially for the *s*-like dot valence states. This is due to the fact that the *s*-like dot state is more sensitive to the valence-conduction coupling. This shows that in order to have a correct prediction about the *s*/*p* level order, *inclusion of the three highest bulk valence bands is insufficient even if the bulk dispersions of these three bands are exact*. Like our direct pseudopotential result, a recent tight-binding calculation[54] on Si dots including the valence-conduction coupling also gives a *s*-like HODO state except for very small dots (less than 87 atoms) where the surface effect can not be neglected. Not surprisingly, in Table V, when we replace the pseudopotential bulk bands by an equivalent number of **k·p** bands (column 5), the estimated energy levels seriously differ from column 4 (also from column 2) due to the difference in bulk band dispersion.

TABLE IV. Energy levels of the lowest conduction state of spherical InP quantum dots as calculated by the direct pseudopotential method [Eq. (5)], and as estimated using projection coefficients with different M_b and bulk dispersions [Eq. (27)]. The energy levels are given relative to the bulk VBM energy, in units of eV.

Diameter *D* (Å)	Direct pseudo	Estimated using projection coefficients		
		8 pseudo[a]	1 pseudo[b]	1 **k·p**[c]
20.2	2.39	2.48	2.54	4.00
28.0	2.21	2.22	2.22	2.85
34.8	1.99	2.01	2.04	2.49

[a]Using $M_b=8$ and pseudopotential bulk dispersion.
[b]Using $M_b=1$ and the pseudopotential dispersion of the lowest bulk conduction band.
[c]Using $M_b=1$ and the **k·p** dispersion of the lowest bulk conduction band.

E. Improving k·p performances for InP dots

We have seen that **k·p** errors for dots evolve from (i) restricted size of basis set, and (ii) incorrect bulk dispersion. They could, however, also evolve from (iii) the use of isotropic bands.

We have studied how important the anisotropic effect due to $\gamma_2\neq\gamma_3$ is on the 6×6 **k·p** calculation of dots. This is calculated for InP using $\gamma_1=4.86$, $\gamma_2=1.37$, and $\gamma_3=1.85$,

TABLE V. Energy levels of valence states of InP dots as obtained by direct pseudopotential method, and as estimated using projection coefficients with different M_b and bulk dispersions [Eq. (27)]. For each dot, the first line is for the *s*-like state while the second line is for the *p*-like state. The energy levels are relative to the bulk VBM energy, in units of eV.

Diameter *D* (Å)	Direct pseudo	Estimated using projection coefficient		
		8 pseudo[a]	3 pseudo[b]	3 **k·p**[c]
20.2	−0.47	−0.46	−0.763	−1.77
	−0.63	−0.64	−0.757	−1.39
28.0	−0.23	−0.26	−0.488	−1.07
	−0.31	−0.34	−0.487	−0.90
34.8	−0.17	−0.19	−0.344	−0.69
	−0.22	−0.24	−0.306	−0.47

[a]Using pseudopotential dispersion of the lowest 8 bulk bands.
[b]Using pseudopotential dispersion of the highest 3 bulk valence bands.
[c]Using **k·p** dispersion of the highest 3 bulk valence bands.

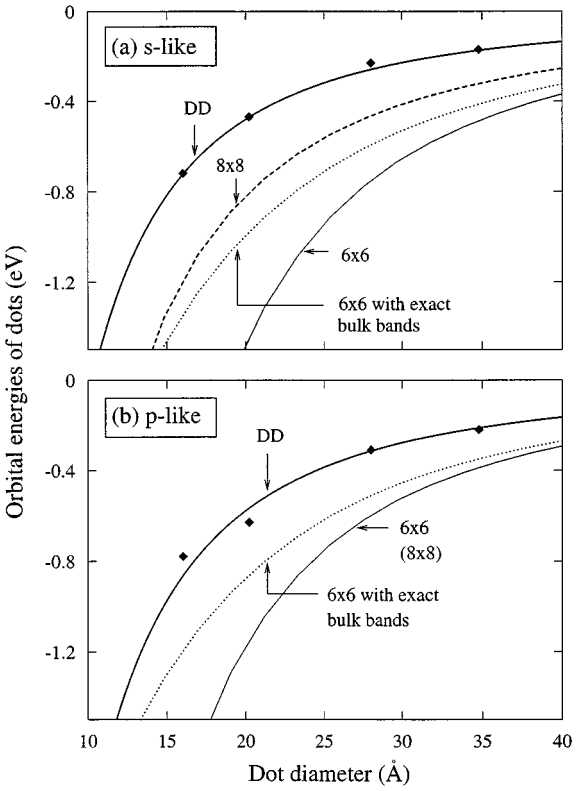

FIG. 7. The orbital energies of the two highest valence orbits of InP dots as calculated by the 8×8 $\mathbf{k}\cdot\mathbf{p}$ model ($\gamma_1'=1.42$, $\overline{\gamma_2'}=-0.062$, $E_p=14.98$, $\alpha=1.00$), the standard 6×6 model ($\gamma_1=4.86$, $\overline{\gamma_2}=1.66$, $\Delta_0=0$), the 6×6 model but with pseudopotential bulk band dispersion, and via direct diagonalization (DD): (a) the s-like dot valence state; (b) the p-like dot valence state. Diamond symbols represent direct diagonalization results, and lines connecting these symbols are guides for eyes.

derived from our pseudopotential bulk band structure. The 6×6 $\mathbf{k}\cdot\mathbf{p}$ Hamiltonian is diagonalized using the basis of $|F,F_z,J,L\rangle_{\theta,\phi}j_L(k_{Lm}r)$, where $k_{Lm}=X_{Lm}/R$ and X_{Lm} is the mth node of $j_L(x)$ [i.e., $j_L(X_{Lm})=0$]. The matrix elements are calculated using the reduced-matrix-element technique.[44,55] The converged results using sufficient number of bases are shown in Table VI in comparison with the isotropically approximated results obtained with $\gamma_2=\gamma_3=\overline{\gamma_2}$. We see that the errors due to isotropic approximation are very small for spherical dots.

TABLE VI. Energies of the valence states of $In_{456}P_{435}$ dot ($D=34.8$ Å) calculated by different $\mathbf{k}\cdot\mathbf{p}$ models and bulk dispersions. The orbital energies are given in units of eV relative to the bulk VBM.

Approach	s-like state	p-like state
Direct diagonalization	−0.172	−0.216
6×6 $\mathbf{k}\cdot\mathbf{p}$ (isotropic)[a]	−0.487	−0.388
6×6 $\mathbf{k}\cdot\mathbf{p}$ (anisotropic)[b]	−0.470	−0.381
8×8 $\mathbf{k}\cdot\mathbf{p}$ (isotropic)[c]	−0.322	−0.388
6×6 $\mathbf{k}\cdot\mathbf{p}$[d]	−0.413	−0.349

[a]Using $\gamma_1=4.86$, $\overline{\gamma_2}=1.66$.
[b]Using $\gamma_1=4.86$, $\gamma_2=1.37$, $\gamma_3=1.85$.
[c]Using $\gamma_1'=1.42$, $\overline{\gamma_2'}=-0.062$, $E_p=14.98$, $\alpha=1.0$.
[d]Using exact pseudopotential bulk dispersions.

To examine error (i), an isotropically-averaged 8×8 $\mathbf{k}\cdot\mathbf{p}$ Hamiltonian was solved for InP dots by variational diagonalization, using a method similar to that one for anisotropic 6×6 $\mathbf{k}\cdot\mathbf{p}$ approach.[44,55] We use the 8×8 Luttinger parameters $\gamma_1'=1.42$, $\overline{\gamma_2'}=-0.062$, $E_p=14.98$, and $\alpha=1.0$ derived from the 6×6 $\mathbf{k}\cdot\mathbf{p}$ parameters (see Appendix B). We find that for the bulk band structure, the 8×8 lh dispersion is much improved as shown in Fig. 2 while the 8×8 hh dispersion is not changed in comparison with the 6×6 $\mathbf{k}\cdot\mathbf{p}$ result, since the hh does not couple with the conduction band. The 8×8 $\mathbf{k}\cdot\mathbf{p}$ valence state energies of dots are illustrated in Fig. 7 and Table VI. We see that the 8×8 model significantly improves the energy of the s-like dot valence state compared to direct diagonalization result, however, it does not change the energy of the p-like dot valence state. This is due to the fact that the s-like state is made of both lh and hh bands, but the p-like state is made of only the hh band. For dot radius below 38 Å, the s/p order of the 8×8 $\mathbf{k}\cdot\mathbf{p}$ model is the same as the direct diagonalization, although the individual energy value is still quite different from the more exact one. For dot radius above 38 Å, the p-like state moves above the s-like state.

We next study how much improvement can be gained by improving (ii). We do this by 6×6 $\mathbf{k}\cdot\mathbf{p}$, using in Eq. (18) the (isotropically-averaged) *exact* pseudopotential dispersion $\epsilon_{nk}^{\rm iso}$ instead of the bulk 6×6 $\mathbf{k}\cdot\mathbf{p}$ dispersion. The results are also shown in Fig. 7 and Table VI. The errors in the energy of the p-like state have been reduced by $\sim50\%$. The same procedure can also be applied to the s-like state. The resulting energy is also much improved from the original 6×6 $\mathbf{k}\cdot\mathbf{p}$ result. Thus, the 6×6 $\mathbf{k}\cdot\mathbf{p}$ with exact bulk dispersion can give much better results than the 6×6 $\mathbf{k}\cdot\mathbf{p}$ with improper bulk dispersion. However, the error compared to the direct diagonalization pseudopotential result is still significant, due to the inadequacy of describing the wave function by a small, Γ-only bulk basis (Fig. 1). While the dispersion relation $\epsilon_{nk}^{\mathbf{k}\cdot\mathbf{p}}$ can be brought into agreement with pseudopotential result by simply using $\mathbf{k}$-dependent coefficients of the $\mathbf{k}\cdot\mathbf{p}$ model Hamiltonian in Eqs. (8) and (9), the inability to describe the off-Γ Bloch wave function is more fundamental, stemming from a too small basis set. This can only be solved[24] by including more bases than 8×8 $\mathbf{k}\cdot\mathbf{p}$ model.

F. Bulk CdSe and CdSe quantum dots

CdSe is stable in the wurzite structure. However, most $\mathbf{k}\cdot\mathbf{p}$ studies on CdSe quantum dots[2,15] assume a zincblende lattice. In order to parallel these studies (and also to compare CdSe with InP), we also assume a zincblende lattice. The pseudopotential-calculated effective masses and the ensuing Luttinger parameters for zinc-blende CdSe are listed in Table I. Since Secs. IV A–D already give a detailed discussion on the comparison between $\mathbf{k}\cdot\mathbf{p}$ and pseudopotential results on InP, we emphasize here only the difference with respect to CdSe.

Figure 8 shows the bulk band structure of zinc-blende CdSe, as calculated by the $\mathbf{k}\cdot\mathbf{p}$ (with parameters in Table I) and by the direct-diagonalization pseudopotential method.

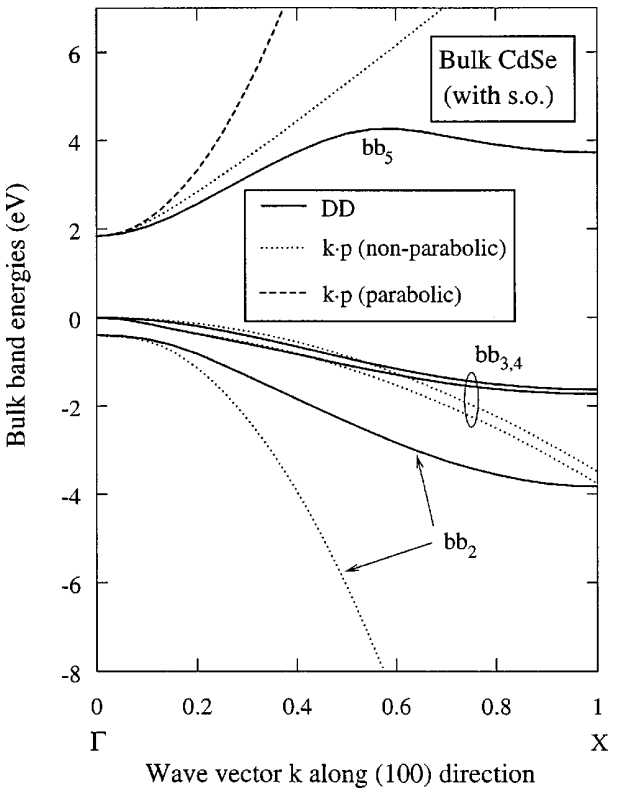

FIG. 8. Band dispersions of bulk CdSe along the ΓX direction as calculated by pseudopotential direct diagonalization (DD, solid lines) and by the 6×6 (for valence using $\gamma_1=2.52$, $\overline{\gamma_2}=0.83$, $\Delta_0=0.42$ eV) and 2×2 (for conduction) $\mathbf{k}\cdot\mathbf{p}$ model (dotted lines). For the conduction band, the single-band parabolic $\mathbf{k}\cdot\mathbf{p}$ dispersion is also shown in dashed line. All curves are calculated with spin-orbit coupling.

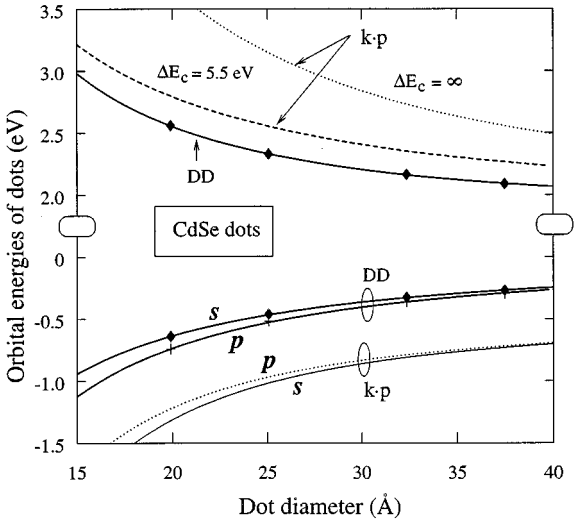

FIG. 9. The orbital energies of the lowest conduction state and of the two highest valence states of CdSe dots. Diamond and cross symbols correspond to *s*- and *p*-like levels, respectively, as calculated by direct diagonalization (DD). The thick solid lines are guides for the eye. For the dot conduction state in the $\mathbf{k}\cdot\mathbf{p}$ model, we show results calculated both with an infinite barrier (dotted line) and with a finite barrier (dashed line). For the dot valence states, the $\mathbf{k}\cdot\mathbf{p}$ curves of both *s*-like (thin solid line) and *p*-like (dotted line) states are down-shifted by 0.5 eV for clarity of display.

By comparing Fig. 8 (CdSe) with Fig. 2 (InP), it can be seen that, the energy difference between the $\mathbf{k}\cdot\mathbf{p}$ and the pseudopotential bulk valence bands is generally smaller in CdSe than in InP. This is due to the more ionic character of CdSe, which flattens the band dispersion and thus diminishes the

TABLE VII. Band contributions $\widetilde{A}_i(n)$ [Eq. (26)] of CdSe bulk band with index *n* in forming the wave functions of dots. The contributions from spin-split bands are summed, and the sum is assigned to one-band contribution in order to facilitate comparison with InP.

Dot size	Bulk band	Projection on LUDO (%)	Projection on *s*-like HODO (%)	Projection on *p*-like HODO (%)
$Cd_{68}Se_{79}$	1	1.93	0.45	0.29
($D=19.9$ Å)	2	4.63	10.96	2.52
	3+4	1.85	85.40	94.46
	5	88.70	0.90	0.59
	6+7+8	1.96	1.04	0.97
	all other	0.93	1.25	1.17
$Cd_{312}Se_{321}$	1	0.92	0.32	0.27
($D=32.4$ Å)	2	2.45	6.08	1.11
	3+4	1.60	91.01	96.30
	5	93.77	0.58	0.39
	6+7+8	0.63	0.82	0.77
	all other	0.63	1.19	1.16
$Cd_{484}Se_{495}$	1	0.75	0.30	0.25
($D=37.5$ Å)	2	2.19	4.67	0.90
	3+4	1.65	92.57	96.53
	5	94.35	0.50	0.39
	6+7+8	0.52	0.78	0.76
	all other	0.54	1.18	1.17

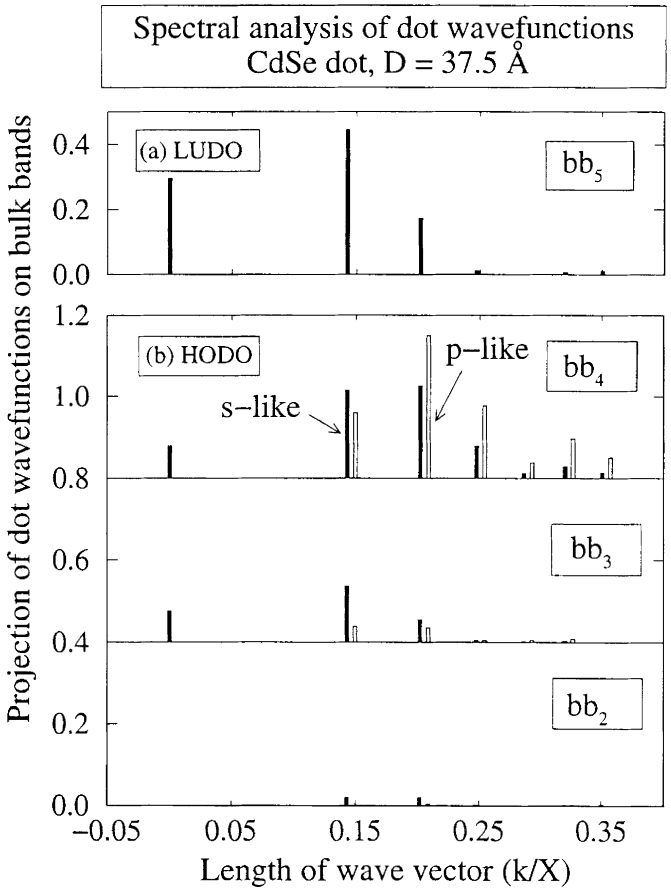

FIG. 10. Projection amplitude $|A_i(n\mathbf{k})|^2$ [see Eq. (25)] showing how much the bulk states $|n\mathbf{k}\rangle$ participate in forming the following states $|i\rangle$ of CdSe dot with 37.5 Å diameter: (a) the lowest unoccupied dot orbit (LUDO); (b) two highest occupied dot orbits (HODO's) with s-like symmetry (filled bars) and p-like symmetry (unfilled bars), where the unfilled bars are slightly shifted horizontally and the projections from different bulk bands to the HODO's are shifted vertically for clarity of display. Here, the bulk bands bb_n are denoted by an index n in the increasing order of energy.

energy difference between $\mathbf{k}\cdot\mathbf{p}$ bands relative to the exact ones. Nevertheless, the $\mathbf{k}\cdot\mathbf{p}$ bulk bands depart significantly from the pseudopotential bands away from the Brillouin-zone origin.

Figure 9 compares the $\mathbf{k}\cdot\mathbf{p}$ and the direct-diagonalization results on the orbital energies of CdSe dots of different sizes. For the LUDO, we see that (i) the infinite barrier $\mathbf{k}\cdot\mathbf{p}$ model predicts much higher confinement energies than the exact diagonalization method, while the finite barrier $\mathbf{k}\cdot\mathbf{p}$ calculation improves the result. (ii) Using pseudopotential-derived $\mathbf{k}\cdot\mathbf{p}$ parameters (Table I), we find that, similar to InP, the HODO in $\mathbf{k}\cdot\mathbf{p}$ calculation is p-like while the HODO in pseudopotential calculation is s-like. This holds using our *bulk*-derived $\mathbf{k}\cdot\mathbf{p}$ parameters $\gamma_1=2.52$ and $\overline{\gamma_2}=0.83$ (Table I). Using instead the $\mathbf{k}\cdot\mathbf{p}$ parameters[2] fit by Norris and Bawendi to the *experimental data on dots* ($\gamma_1=2.04$, $\overline{\gamma_2}=0.58$) gives the s-like level above the p-like level just like our direct diagonalization. While the two sets of parameters give similar effective masses (see Table II), the ensuing electronic structures of dots can be, however, quite different. This illustrates how sensitive the $\mathbf{k}\cdot\mathbf{p}$ calculations are to the Luttinger parameters for CdSe dots as pointed out by Richard *et al.*[15] (iii) The overall agreement between the $\mathbf{k}\cdot\mathbf{p}$ and the direct diagonalization results for valence states is better in CdSe dots (Fig. 9) than in InP dots (Fig. 3).

The bulk band contribution $\widetilde{A}_i(n)$ [Eq. (26)] to the near-edge states of CdSe dots are illustrated in Table VII. In this table, the contributions from two bulk bands split by spin-orbit coupling are summed, and the summed contribution is assigned to one band in order to facilitate a direct comparison with Table III for InP dots. The projection distributions in Table VII for CdSe are quite similar to those in Table III for InP, i.e., the lowest dot conduction state has a dominant contribution from the lowest bulk conduction band, while the dot valence states come mainly from the three highest bulk valence bands. The significant difference is that, the contribution of the bulk band bb_2 to the s-like dot valence state in CdSe is significantly smaller than in InP (Table III). This is due to the large spin-orbit splitting Δ_0 in CdSe, moving bb_2 to deeper energies. Since bb_2 has a large error in bulk $\mathbf{k}\cdot\mathbf{p}$ (Fig. 8), the smaller participation of bb_2 in forming the dot's s-like state alleviates the $\mathbf{k}\cdot\mathbf{p}$ error in this dot state.

The projection amplitude into specific bulk bands and different $\mathbf{k}$ points are shown in Fig. 10. Again, we see that the bulk band bb_2 in CdSe (Fig. 10) does not contribute as significantly as in InP (Fig. 5) in forming the dot s-like valence state.

The above comparison between CdSe and InP quantum dots shows that the $\mathbf{k}\cdot\mathbf{p}$ performance on CdSe dots is better than on InP dots for two reasons: (i) Considering the bulk band structures, the more ionic nature of CdSe flattens the band dispersion relation, so the overall difference between the predictions of the $\mathbf{k}\cdot\mathbf{p}$ bulk bands and the pseudopotential bulk bands is smaller; (ii) Considering the bulk wave function contribution to the dot states, the large spin-orbit splitting in CdSe moves the poorly-described bulk band bb_2 to deeper energies, and reduces its contribution (and error) to the dot's s-like state.

V. SUMMARY AND CONCLUSIONS

The $\mathbf{k}\cdot\mathbf{p}$ method and the direct-diagonalization pseudopotential method are used to calculate in parallel the electronic structures of InP and CdSe quantum dots. By using the pseudopotential-derived $\mathbf{k}\cdot\mathbf{p}$ Luttinger parameters, we are able to find out the sources of $\mathbf{k}\cdot\mathbf{p}$ errors in quantum-dot electronic structure calculation (thus the way to improve the $\mathbf{k}\cdot\mathbf{p}$ performance). Our main conclusions are the following:

(i) The $\mathbf{k}\cdot\mathbf{p}$ approach predicts that the highest occupied dot orbit has a p-like symmetry, while the direct diagonalization approach predicts that it has a dominant s-like symmetry with parity mixing. This holds for very large dots.

(ii) The $\mathbf{k}\cdot\mathbf{p}$ predicts that the second conduction state in small InP dots is Γ-like, while direct diagonalization shows that it is L-like.

(iii) The $\mathbf{k}\cdot\mathbf{p}$ approach generally overestimates the confinement energies of both valence and conduction states of quantum dots.

(iv) We demonstrated, via the wave function projection, that the $\mathbf{k}\cdot\mathbf{p}$ errors in dots originate from two main sources (a) the use of restricted basis set, and (b) the $\mathbf{k}\cdot\mathbf{p}$ errors in describing the bulk band structures.

(v) Error (a) occurs because the off-Γ Bloch states can not

be accurately described by a small number of Γ-like Bloch basis set. This kind of error can only be reduced by increasing the size of the basis.

(vi) Error (b) results specifically from (1) the fact that the *s*-like dot valence state has a significant contribution from bulk band bb_2, which the $\mathbf{k}\cdot\mathbf{p}$ model predicts at too deep energies; (2) the fact that the *p*-like dot valence state has large contribution from off-Γ part of bulk band structure whose dispersion is poorly described by $\mathbf{k}\cdot\mathbf{p}$; (3) inclusion of the valence-conduction coupling affects differently the energies of the *s*-like and *p*-like dot states, thus changing their energy separation.

(vii) $\mathbf{k}\cdot\mathbf{p}$ errors in CdSe dots appear to be smaller than in InP dots due to the more ionic nature and the large spin-orbit splitting of CdSe material.

(viii) The wave function and energy analysis suggests that in order to improve the $\mathbf{k}\cdot\mathbf{p}$ performance in quantum dots, one needs to (1) correct the second lowest bulk band, and make it less deeper; (2) couple the valence bands to the conduction bands. However, direct-diagonalization provides an accurate and practical replacement to the $\mathbf{k}\cdot\mathbf{p}$.

ACKNOWLEDGMENTS

We thank S. H. Wei, Y. Zhang, and J. Kim for helpful discussions, and thank A. Franceschetti for his comments on the manuscript. This work was supported by the U.S. Department of Energy, OER-BES, under Grant No. DE-AC36-83CH10093.

APPENDIX A: $\mathbf{k}\cdot\mathbf{p}$ HAMILTONIAN MATRIX FOR BULK IN $|J,J_z\rangle$ BASES

Using the bases $|J,J_z\rangle$ in Eq. (12), the $\mathbf{k}\cdot\mathbf{p}$ Hamiltonian [Eq. (7)] can be obtained, after a unitary transform of the matrix in Eq. (8), as follows:

$$
\begin{array}{cccccccc}
\left|\frac{1}{2},\frac{1}{2}\right\rangle_e & \left|\frac{1}{2},-\frac{1}{2}\right\rangle_e & \left|\frac{3}{2},\frac{3}{2}\right\rangle_h & \left|\frac{3}{2},\frac{1}{2}\right\rangle_h & \left|\frac{3}{2},-\frac{1}{2}\right\rangle_h & \left|\frac{3}{2},-\frac{3}{2}\right\rangle_h & \left|\frac{1}{2},\frac{1}{2}\right\rangle_h & \left|\frac{1}{2},-\frac{1}{2}\right\rangle_h \\
Y & 0 & -\sqrt{3}V^* & \sqrt{2}U & V & 0 & U & -\sqrt{2}V \\
 & Y & 0 & V^* & \sqrt{2}U & \sqrt{3}V & -\sqrt{2}V^* & U \\
 & & -T-Q & -S & R & 0 & -\frac{1}{\sqrt{2}}S & -\sqrt{2}R \\
 & & & -T+Q & 0 & -R & \sqrt{2}Q & \sqrt{\frac{3}{2}}S \\
 & & & & -T+Q & -S & -\sqrt{\frac{3}{2}}S^* & \sqrt{2}Q \\
 & & & & & -T-Q & \sqrt{2}R^* & -\frac{1}{\sqrt{2}}S^* \\
 & & & & & & Z & 0 \\
 & & & & & & 0 & Z
\end{array}
\tag{A1}
$$

Here, the related parameters $\{Y,U,V,T,Q,R,S,Z\}$ are functions of the ensemble $\{\gamma_1,\ \gamma_2,\ \gamma_3,\ A',\ P$ and $\Delta_0\}$ in Eqs. (9) and (10), and are explicitly written as

$$Y=\epsilon_{c,0}+A'(k_x^2+k_y^2+k_z^2)=\epsilon_g+A'(k_x^2+k_y^2+k_z^2),$$

$$U=\sqrt{\tfrac{1}{3}}iPk_z,$$

$$V=\sqrt{\tfrac{1}{6}}iP(k_x-ik_y),$$

$$T=+\frac{\Delta_0}{3}+\tfrac{1}{2}\gamma_1(k_x^2+k_y^2+k_z^2)=\tfrac{1}{2}\gamma_1(k_x^2+k_y^2+k_z^2),$$

$$Q=\tfrac{1}{2}\gamma_2(k_x^2+k_y^2-2k_z^2),$$

$$R=-\frac{\sqrt{3}}{2}[\gamma_2(k_x^2-k_y^2)-2i\gamma_3k_xk_y],$$

$$S=\sqrt{3}\gamma_3k_z(k_x-ik_y),$$

$$Z=-\tfrac{2}{3}\Delta_0-\tfrac{1}{2}\gamma_1(k_x^2+k_y^2+k_z^2)=-\Delta_0-\tfrac{1}{2}\gamma_1(k_x^2+k_y^2+k_z^2),\tag{A2}$$

where ϵ_g is band gap. After the spin-orbit coupling, the valence-band maximum becomes $+\frac{1}{3}\Delta_0$, and is taken as energy zero point in the most right-hand-side equations for parameters Y, T, and Z. Equations (A1) and (A2) constitute the 8×8 bulk $\mathbf{k}\cdot\mathbf{p}$ method, cast in $|J,J_z\rangle$ representation.

APPENDIX B: SUBMATRICE OF ISOTROPIC $\mathbf{k}\cdot\mathbf{p}$ HAMILTONIAN

In the irreducible representation $|F,F_z,J,L\rangle$ [Eq. (15)], the isotropic Hamiltonian (with $\gamma_2=\gamma_3=\overline{\gamma_2}$) is block-diagonal for different $\{F,F_z\}$. By using Eqs. (13) and (15) and Eq. (A1), the submatrix H_{F,F_z} corresponding to $F=\frac{1}{2}$

can be obtained, by some derivation, as

$$H_{\frac{1}{2},\pm\frac{1}{2}}=\begin{pmatrix} H_1 & \\ & H_2 \end{pmatrix},$$

$$H_{\{1;2\}}=\begin{bmatrix} |\tfrac{1}{2},\{0;1\}\rangle & |\tfrac{3}{2},\{1;2\}\rangle & |\tfrac{1}{2},\{1;0\}\rangle \\ \epsilon_g+\tfrac{1}{2}k^2 & -\sqrt{\tfrac{2}{3}}iPk & -\sqrt{\tfrac{1}{3}}iPk \\ & -(\gamma_1+2\bar{\gamma}_2)\dfrac{k^2}{2} & -\sqrt{2}\bar{\gamma}_2k^2 \\ & & -\Delta_0-\gamma_1\dfrac{k^2}{2} \end{bmatrix}, \tag{B1}$$

where $k^2=k_x^2+k_y^2+k_z^2$ is the length of wave vector $\mathbf{k}$. In H_1 and H_2, the bases $|F,F_z,J,L\rangle$ [abbreviated as $|J,L\rangle$ due to fixed $\{F,F_z\}$] are given in the first row. Note that, in the isotropic approximation, the Hamiltonian matrix elements depends only on the amplitude of $\mathbf{k}$, not its direction. The Hamiltonian submatrix for $F=\frac{3}{2}$ is obtained as

$$H_{\frac{3}{2},\pm\frac{3}{2}\ \text{or}\ \pm\frac{1}{2}}=\begin{pmatrix} H_3 & \\ & H_4 \end{pmatrix},$$

$$H_3=\begin{bmatrix} |\tfrac{1}{2},1\rangle & |\tfrac{3}{2},0\rangle & |\tfrac{3}{2},2\rangle & |\tfrac{1}{2},2\rangle \\ \epsilon_g+\tfrac{1}{2}k^2 & \sqrt{\tfrac{1}{3}}iPk & -\sqrt{\tfrac{1}{3}}iPk & -\sqrt{\tfrac{1}{3}}iPk \\ & -\gamma_1\dfrac{k^2}{2} & \bar{\gamma}_2k^2 & \bar{\gamma}_2k^2 \\ & & -\gamma_1\dfrac{k^2}{2} & -\bar{\gamma}_2k^2 \\ & & & -\Delta_0-\gamma_1\dfrac{k^2}{2} \end{bmatrix}, \tag{B2}$$

$$H_4=\begin{bmatrix} |\tfrac{1}{2},2\rangle & |\tfrac{3}{2},1\rangle & |\tfrac{3}{2},3\rangle & |\tfrac{1}{2},1\rangle \\ \epsilon_g+\tfrac{1}{2}k^2 & \sqrt{\tfrac{1}{15}}iPk & -\sqrt{\tfrac{3}{5}}iPk & -\sqrt{\tfrac{1}{3}}iPk \\ & (-\gamma_1+\tfrac{8}{5}\bar{\gamma}_2)\dfrac{k^2}{2} & \tfrac{3}{5}\bar{\gamma}_2k^2 & \sqrt{\tfrac{1}{5}}\bar{\gamma}_2k^2 \\ & & -(\gamma_1+\tfrac{8}{5}\bar{\gamma}_2)\dfrac{k^2}{2} & -\dfrac{3}{\sqrt{5}}\bar{\gamma}_2k^2 \\ & & & -\Delta_0-\gamma_1\dfrac{k^2}{2} \end{bmatrix}. \tag{B3}$$

In the 6×6 $\mathbf{k}\cdot\mathbf{p}$ model, we decouple the valence bands from the conduction bands, i.e., take $P=0$ in Eqs. (B1)–(B3) for valence states.

The relationship between the 6×6 Luttinger parameters and the effective masses follows Eqs. (A1.c)–(A1.f) in Ref. 23, i.e.,

$$m_{hh}^{-1}(001)=\gamma_1-2\gamma_2,\quad m_{lh}^{-1}(001)=\gamma_1+2\gamma_2, \tag{B4}$$

$$m_{hh}^{-1}(111)=\gamma_1-2\gamma_3,\quad m_{lh}^{-1}(111)=\gamma_1+2\gamma_3,$$

for nonvanishing spin-orbit coupling Δ_0, and

$$\begin{aligned} m_{hh}^{-1}(001)&=\gamma_1-2\gamma_2,\quad m_{lh}^{-1}(001)=\gamma_1+4\gamma_2, \\ m_{hh}^{-1}(111)&=\gamma_1-2\gamma_3,\quad m_{lh}^{-1}(111)=\gamma_1+4\gamma_3, \end{aligned} \tag{B5}$$

for vanishing spin-orbit coupling Δ_0. It is found that the Luttinger parameters obtained from the pseudopotential cal-

culations with ($\Delta_0 \neq 0$) and without spin-orbit coupling ($\Delta_0 = 0$) are very close (with difference less than 5%) for InP. The four equations with three unknowns give γ_1 value with an uncertainty of less than 1%. The relationships between the 8×8 and the 6×6 **k**·**p** parameters, providing consistent hole effective masses, are:

$$\gamma_1'(8\times 8) = \gamma_1(6\times 6) - \frac{2}{3}\frac{P^2}{\epsilon_g},$$

$$\overline{\gamma_2'}(8\times 8) = \overline{\gamma_2}(6\times 6) - \frac{1}{3}\frac{P^2}{\epsilon_g}.$$

[1] M. Nirmal, D. J. Norris, M. Kuno, M. G. Bawendi, Al. L. Efros, and M. Rosen, Phys. Rev. Lett. **75**, 3728 (1996).
[2] D. J. Norris and M. G. Bawendi, Phys. Rev. B **53**, 16 338 (1996).
[3] M. Chamarro, C. Gourdon, P. Lavallard, O. Lublinskaya, and A. I. Ekimov, Phys. Rev. B **53**, 1336 (1996).
[4] O. Wind, F. Gindele, and U. Woggon, J. Lumin. **72-74**, 300 (1997).
[5] O. I. Micic, J. Sprague, Z. Lu, and A. J. Nozik, Appl. Phys. Lett. **68**, 3150 (1996).
[6] O. I. Micic, H. M. Cheong, H. Fu, A. Zunger, J. R. Sprague, A. Mascarenhas, and A. J. Nozik, J. Phys. Chem. **101**, 4904 (1997).
[7] U. Banin, G. Cerullo, A. A. Guzelian, C. J. Bardeen, A. P. Alivisatos, and C. V. Shank, Phys. Rev. B **55**, 7059 (1997).
[8] A. A. Guzelian, U. Banin, A. V. Kadavanich, X. Peng, and A. P. Alivisatos, Appl. Phys. Lett. **69**, 1432 (1996); U. Banin, J. C. Lee, A. A. Guzelian, and A. P. Alivisatos (unpublished).
[9] S. Fafard, D. Leonard, J. L. Merz, and P. M. Petroff, Appl. Phys. Lett. **65**, 1388 (1994).
[10] M. Grundmann, J. Christen, N. N. Ledenstov, and D. Bimberg, Phys. Rev. Lett. **74**, 3043 (1995).
[11] K. H. Schmidt, G. Medeiros-Ribeiro, M. Oestreich, P. M. Petroff, and G. H. Dohler, Phys. Rev. B **54**, 11 346 (1996).
[12] J. Y. Marzin, J. M. Gerard, A. Israel, D. Barrier, and G. Bastard, Phys. Rev. Lett. **73**, 716 (1994).
[13] M. A. Cusack, P. R. Briddon, and M. Jaros, Phys. Rev. B **54**, R2300 (1996).
[14] H. Jiang and J. Singh, Phys. Rev. B **56**, 4696 (1997).
[15] T. Richard, P. Lefebvre, H. Mathieu, and J. Allegre, Phys. Rev. B **53**, 7287 (1996).
[16] G. B. Grigoryan, E. M. Kazaryan, Al. L. Efros, and T. V. Yazeva, Fiz. Tverd. Tela. **32**, 1772 (1990) [Sov. Phys. Solid State **32**, 1031 (1990)].
[17] J. M. Luttinger and W. Kohn, Phys. Rev. **97**, 869 (1955).
[18] E. O. Kane, in *Semiconductor and Semimetals*, edited by R. K. Willardson and A. C. Beer (Academic, New York, 1966), Vol. I, p. 75.
[19] P. C. Sercel and K. J. Vahala, Phys. Rev. B **42**, 3690 (1990).
[20] M. Grundmann, O. Stier, and D. Bimberg, Phys. Rev. B **52**, 11 969 (1996).
[21] H. Fu and A. Zunger, Phys. Rev. B **56**, 1496 (1997).
[22] M. Willatzen, M. Cardona, and N. E. Christensen, Phys. Rev. B **50**, 18 054 (1994).
[23] D. M. Wood and A. Zunger, Phys. Rev. B **53**, 7949 (1996).
[24] L. W. Wang and A. Zunger, Phys. Rev. B **54**, 11 417 (1996).
[25] L. M. Ramaniah and S. V. Nair, Phys. Rev. B **47**, 7132 (1993).
[26] D. L. Smith and C. Mailhiot, Rev. Mod. Phys. **62**, 173 (1990).
[27] A. Zunger, C. Y. Yeh, L. W. Wang, and S. B. Zhang, in *International Conference on Physics and Semiconductors*, edited by D. J. Lockwood (World Scientific, Singapore, 1995).
[28] P. Guyot-Sionnest (private communication).
[29] W. Kohn and L. J. Sham, Phys. Rev. **140**, A1133 (1965); J. Perdew and A. Zunger, Phys. Rev. B **23**, 5048 (1981).
[30] J. R. Chelikowsky and M. L. Cohen, Phys. Rev. B **14**, 556 (1976).
[31] L. W. Wang and A. Zunger, Phys. Rev. B **51**, 17 398 (1995).
[32] H. Fu and A. Zunger, Phys. Rev. B **55**, 1642 (1997).
[33] J. Ihm, A. Zunger, and M. L. Cohen, J. Phys. C **12**, 4409 (1979).
[34] L. W. Wang and A. Zunger, J. Chem. Phys. **100**, 2394 (1994); J. Phys. Chem. **94**, 2158 (1994).
[35] K. A. Mader, L. W. Wang, and A. Zunger, Phys. Rev. Lett. **74**, 2555 (1995).
[36] A. Franceschetti and A. Zunger, Phys. Rev. Lett. **78**, 915 (1997); Phys. Rev. B **52**, 14 664 (1995).
[37] P. Löwdin, J. Math. Phys. **3**, 969 (1962).
[38] T. B. Bahder, Phys. Rev. B **41**, 11 992 (1990).
[39] G. A. Baraff and D. Gershoni, Phys. Rev. B **43**, 4011 (1991); D. Gershoni, C. H. Henry, and G. A. Baraff, IEEE J. Quantum Electron. **29**, 2433 (1993).
[40] S. S. Li, J. B. Xia, Z. L. Yuan, Z. Y. Xu, W. Ge, X. R. Wang, Y. Wang, J. Wang, and L. L. Chang, Phys. Rev. B **54**, 11 575 (1996).
[41] A. Baldereschi and N. O. Lipari, Phys. Rev. B **8**, 2697 (1973).
[42] L. D. Landau and E. M. Lifshitz, *Quantum Mechanics* (Pergamon, Oxford, 1977), p. 431.
[43] D. I. Chepic, Al. L. Efros, A. I. Ekimov, M. G. Ivanov, V. A. Kharchenko, I. A. Kudryavtsev, and T. V. Yazeva, J. Lumin. **47**, 113 (1990).
[44] A. Baldereschi and N. O. Lipari, Phys. Rev. B **9**, 1525 (1974).
[45] P. Rochon and E. Fortin, Phys. Rev. B **12**, 5803 (1975).
[46] Z. Hang, H. Shen, and F. H. Pollak, Solid State Commun. **36**, 15 (1990).
[47] D. Bimberg, K. Hess, N. O. Lipari, J. U. Fischbach, and M. Altarelli, Physica B & C **89**, 139 (1977).
[48] P. Lawaetz, Phys. Rev. B **4**, 3460 (1971).
[49] J. Leotin, R. Barbaste, S. Askenazy, M. S. Skolnick, R. A. Stradling, and J. Tuchendler, Solid State Commun. **15**, 693 (1974).
[50] Yu. M. Sirenko, J. B. Jeon, K. W. Kim, M. A. Littlejohn, and M. A. Stroscio, Phys. Rev. B **53**, 1997 (1996).
[51] C. Hermann and P. Y. Yu, Phys. Rev. B **21**, 3675 (1980).
[52] G. L. Bir and G. E. Pikus, *Symmetry and Strain-Induced Effects in Semiconductors* (Wiley, New York, 1975), p. 469; see also, R. G. Wheeler and J. O. Dimmock, Phys. Rev. **125**, 1805 (1962).
[53] M. V. Rama Krishna and R. A. Friesner, Phys. Rev. Lett. **67**, 629 (1991).
[54] S. Y. Ren, Phys. Rev. B **55**, 4665 (1997).
[55] A. R. Edmonds, *Angular Momentum in Quantum Mechanics*, (Princeton University Press, Princeton, New Jersey, 1960); M. Rotemberg, R. Bivins, N. Metropolis, and J. K. Wooten, *The* 3-*j and* 6-*j Symbols* (Technical Press, Cambridge, Massachusetts, 1959).